

Synergy or Antagonism? Exploring the Interplay of SnO₂ and an N-OMC Carbon Capture Medium for the Electrochemical CO₂ Reduction Towards Formate

Kevin Van Daele^{a,b}, Deema Balalta^c, Saskia Hoekx^{a,c}, Robbe Jacobs^{a,e}, Dr. Nick Daems^a, Dr. Thomas Altantzis^a, Dr. Deepak Pant^{b,d}, Prof. Dr. Tom Breugelmans*^{a,d}

a) Applied Electrochemistry & Catalysis (ELCAT), University of Antwerp, Universiteitsplein 1, 2610 Wilrijk, Belgium

b) Electrochemistry Excellence Centre, Materials & Chemistry unit, Flemish Institute for Technological Research (VITO), Boeretang 200, 2400 Mol, Belgium

c) Electron Microscopy for Materials Science (EMAT), University of Antwerp, Groenenborgerlaan 171, 2020 Antwerp, Belgium

d) Center for Advanced Process Technology for Urban Resource Recovery (CAPTURE), Frieda Saeystraat 1, 9052 Zwijnaarde, Belgium

e) Design & Synthesis of Inorganic materials for Energy applications (DESINE), University of Hasselt, Agoralaan, 3590 Diepenbeek, Belgium

*corresponding author: tom.breugelmans@uantwerpen.be

Abstract

Closing the anthropogenic carbon cycle by means of the sustainable electrochemical CO₂ reduction (eCO₂R) towards formate (FA) is a promising strategy for CO₂ abatement, clearing the path towards a carbon neutral future. Currently, three possible reaction pathways have been identified for the eCO₂R towards FA, all of which are initiated by the adsorption of CO₂ on the electrocatalyst's surface. Therefore, a possible strategy to enhance the CO₂ availability near the active sites is to combine an active electrocatalyst material (here, SnO₂) with a known carbon capture medium (here, nitrogen-doped ordered mesoporous carbon (N-OMC)). SnO₂ was introduced *in situ* during the N-OMC synthesis, yielding SnO₂-N-OMCs. We approached the state-of-the-art for Sn-based N-doped carbon electrocatalysts in terms of performance under industrially relevant currents with an FE_{FA} of 59% for SnO₂-N-OMC (6) and 61% for SnO₂-N-OMC (2). Moreover, the SnO₂-N-OMC electrocatalysts require a low overpotential, courtesy of the N-OMC support, compared to the state-of-the-art, for the selective conversion of CO₂ towards FA at the industrially relevant current density of 100 mA cm⁻². Additionally, the 24 h stability of the best performing SnO₂-N-OMC electrocatalysts is explored and pulverization/agglomeration and *in situ* SnO₂ reduction are identified as major degradation pathways, allowing future research to be steered more accurately towards more stable Sn-based electrocatalysts

for the eCO₂R towards FA. An optimal combination of both the SnO₂ species and the N-OMC carbon capture medium could result in a synergistic effect, especially when utilization of the N-OMC support material is optimized to morphologically stabilize the SnO₂ active species.

Keywords

Nitrogen doped Ordered Mesoporous Carbon, SnO₂, Degradation Misms, Electrochemical CO₂ Reduction, Formate

1. Introduction

Since the start of the second industrial revolution in the late 19th century, a rapid increase in anthropogenic CO₂ emissions has been supercharging Earth's natural greenhouse effect, making CO₂ Earth's most harmful and prevalent greenhouse gas, bringing about global warming, disrupted weather patterns and an acidification of the oceans¹⁻³. Nonetheless, innovative negative carbon technologies such as Carbon Capture and Storage (CCS) or Carbon Capture and Utilization (CCU) are gaining momentum as they provide a promising strategy for CO₂ abatement, leading to an imperative carbon neutral future⁴⁻⁷. More than two decades ago, Hori *et al.* laid the groundwork for closing the anthropogenic carbon cycle by means of electrochemical CO₂ reduction (eCO₂R) towards value-added chemicals⁸. Utilizing renewable electricity and water, CO₂ is electrocatalytically reduced into various value-added products, such as carbon monoxide (CO), formate (FA, HCOO⁻), methanol (CH₃OH) and ethylene (C₂H₄)⁹. Among these reaction products, formate, a 2-electron transfer liquid product, and CO, a gaseous product, currently have the potential to generate the highest revenue per mole of consumed electrons^{10,11}. Furthermore, FA could play an important role as a means for future energy storage due to its use as a hydrogen or CO carrier¹². Since Hori's pioneering work, numerous excellent metal-based electrocatalysts, such as Pb, Hg, Cd, Tl, Co, Sb, Bi, In and Sn have been found to be selective for the eCO₂R towards formate^{8,13,14}. While Pb, Hg, Cd and Tl are harmful to the environment and have a high toxicity, Co and Sb-based electrocatalysts have only recently gained attention and are still in the early stages of research¹³. Unlike the aforementioned electrode materials, Bi-, In- and Sn-based electrocatalysts all have a low toxicity, are more environmentally friendly and currently yield the best electrochemical performances for the eCO₂R towards FA¹⁵. Due to their high selectivity (FE_{FA}), low toxicity, non-noble nature, ecological and inexpensive properties, Sn-based electrocatalysts are one of the most interesting candidates for the eCO₂R towards FA¹⁶⁻¹⁸.

Currently, three possible reaction pathways have been identified for the eCO₂R towards FA, all of which are initiated by the adsorption of CO₂ on the electrocatalyst's surface^{18,19}. Deng *et al.* recently uncovered that the rate-determining step (RDS) of these reaction pathways is this first step, the adsorption of CO₂ onto the electrocatalytic active site²⁰. Consequently, in order to enhance the overall eCO₂R, the interaction, i.e. adsorption, between the slightly acidic CO₂ molecules and electrocatalyst surface has to be improved in order to fend off the competing hydrogen evolution reaction (HER) and to yield a high selectivity and productivity. This is frequently achieved in literature by incorporating nitrogen functional groups into carbon support materials²¹. Nitrogen-doped (N-doped) porous carbon materials are frequently used for efficient CO₂ capture, as the introduction of nitrogen into the carbon matrix increases the surface polarity and basicity, which results in enhanced CO₂ adsorption^{21–23}. Introducing SnO₂, as a selective electrocatalyst towards FA, during the synthesis of N-doped carbons could also prove to simultaneously functionalize the carbon capture medium and facilitate the rate-determining CO₂ adsorption for the eCO₂R towards FA²⁴.

In the state of the art, a few other SnO_x N-doped carbon electrocatalysts with selectivities reaching up to 80% towards formate have been reported^{24–26}. Zhang *et al.*, for example, decorated nitrogen-doped multiwalled carbon nanotubes (N-MWCNTs) with SnO₂ nanoparticles (SnO₂/N-MWCNTs), achieving an FE_{FA} of up to 46% at an applied potential of -0.9 V vs. Ag/AgCl, compared to only 10% for the supporting N-MWCNTs material, indicating that the incorporation of SnO₂ nanoparticles shifts the eCO₂R selectivity towards formate²⁷. These observations were verified by Birdja *et al.*, who revealed the ability of the metal center of metalloprotoporphyrins to tune the selectivity towards FA. In their research, they found that the Faradaic efficiency for formic acid increased with different metal centers, such as In and Sn²⁸. Furthermore, Zhao *et al.*, modified an N-doped carbon nanofiber with Sn species to obtain a tunable electrocatalytic performance towards either CO or formate, depending on the structure of the incorporated Sn species. In their research, they revealed that atomically dispersed Sn species drive the CO₂ conversion towards CO, while Sn nanoparticles promote the electrocatalytic conversion of CO₂ towards formate with a selectivity of 62%²⁹. Moreover, Duarte *et al.* reported a tunable selectivity towards the desired eCO₂R product by altering the embedded transition metal in their metal-nitrogen-doped carbon electrocatalyst. With a partial current density of 70 mA cm⁻², their Sn-N-C catalyst achieved a Faradaic efficiency of 70% towards formate³⁰. Finally, Fu *et al.*, described an electrochemically exfoliated graphene supported 2D confined core-shell structured SnO₂ nanoparticle electrocatalyst, encapsulated into N-doped carbon. The combination of N dopants and a strong particle confinement effect resulted in a high FE_{FA} of 81.2% at -1.2 V²⁴.

Here, N-doped ordered mesoporous carbons (N-OMCs) are functionalized for the eCO₂R towards FA by introducing SnO₂ during the synthesis, yielding SnO₂-N-OMCs. Contrary to previous research, we

wanted to explore the interplay between SnO₂, which is well-known to be selective for the eCO₂R towards FA, and an N-OMC carbon capture medium as support material, which facilitates the rate-determining CO₂ adsorption. We investigated the influence of the introduction of an SnO₂ precursor during the N-OMC synthesis, while simultaneously revealing the influence of the N-OMC carbon capture medium and SnO₂ species on the electrochemical performance and studying their electrocatalytic stability and degradation pathways. We unravelled whether or not combining SnO₂ with an N-OMC carbon capture medium has a synergistic effect because of the enhanced CO₂ adsorption. To realize this, seven different (SnO₂-)N-OMC electrocatalysts were prepared with varying SnO₂ contents, incorporated during various synthesis steps, and with a variable specific surface area (S_{BET}). This allowed us to simultaneously investigate the influence of introducing the SnO₂ species on the morphology of the N-OMC, and more importantly, the influence of the N-OMC support material and SnO₂ species on the electrochemical performance for the eCO₂R towards FA. With a FE_{FA} of 59% for SnO₂-N-OMC (6) and 61% for SnO₂-N-OMC (2), we approached the state-of-the-art for Sn-based N-doped carbon electrocatalysts in terms of performance under industrially relevant currents. Furthermore, the SnO₂-N-OMC electrocatalysts require a lower overpotential, due to the N-OMC support, for the selective (\pm 60%) conversion of CO₂ towards FA at the industrially relevant current density of 100 mA cm⁻². Additionally, the 24 h stability of these best performing SnO₂-N-OMC electrocatalysts is explored and their most predominant degradation mechanisms are identified, allowing future research to be steered towards more stable Sn-based electrocatalysts.

2. Experimental

2.1 Materials

The following chemicals were used as received, without any further purification: acetone (99.5+%, a.r., Chem-Lab), ammonium peroxydisulfate (98%, Alfa Aesar), aniline (99.8%, pure, Acros Organics), 2,3-dihydroxynaphthalene (\geq 98.0%, Sigma-Aldrich), D520 NAFION[®] solution (Ion Power), glycerol (a.r., Fisher Scientific), hydrochloric acid (37%, a.r., Chem-Lab), hydrochloric acid (37%, Honeywell chemicals), hydrofluoric acid (40%, VWR chemicals), hydrogen peroxide (35%, Merck), nitric acid (67-70%, Avantor - J.T.Baker), ICP Multi-element standard solution IV (Merck), pluronic[®] P-123 (PEG-PPG-PEG, average Mn \sim 5.800, Sigma-Aldrich), potassium hydrogen carbonate (99.5+%, v.p., Chem-Lab), potassium hydroxide (85+%, pellets a.r., Chem-Lab), propanol-2 (99.8+%, iso-propanol a.r., Chem-Lab), sodium hydroxide (99+%, pellets a.r., Chem-Lab), tetraethyl orthosilicate (98%, Acros Organics), tin(II) chloride.2aq (98+%, a.r., Chem-Lab), tin plasma standard solution (Sn 1000ppm, Specpure, Alfa Aesar).

2.2 Synthesis

2.2.1 Preparation of the SBA-15 hard template

In a typical SBA-15 synthesis, 1.8 g Pluronic® P-123 and 1.8 g glycerol were stirred overnight in 69 g of a 1 M hydrochloric acid (HCl) aqueous solution, at 35 °C, in a polypropylene (Nalgene®) bottle. Next, 3.87 g tetraethyl orthosilicate (TEOS) was added dropwise to the mixture under vigorous stirring. Subsequently, the mixture was kept at 35 °C for an additional 24 h under static conditions. Afterwards, a hydrothermal treatment was performed at 100 °C for 24 h. Finally, the solid product was collected by filtration, washed with distilled water until a pH 4-5 was obtained, and dried overnight at 80 °C. The resulting white powder was calcined at 550 °C for 6h (1°C min⁻¹) in flowing air, in order to remove the organic structure directing agent (SDA) ^{31,32}.

2.2.2 Fabrication of the SnO₂ nitrogen-doped ordered mesoporous carbon electrocatalyst

SnO₂ N-doped ordered mesoporous carbon (SnO₂-N-OMC) materials were prepared using a two-step procedure (Figure 1), inspired by and adapted from Wang *et al.* ³³ and Sheng *et al.* ³¹, respectively. The SnO₂ precursor (SnCl₂·2H₂O) was included either completely during addition of the aniline or 2,3-dihydroxynaphthalene or divided between both steps, as depicted in figure 1. A detailed overview of the performed syntheses can be found in Table 1.

As a first step, aniline was polymerized inside the pores of the SBA-15 hard template. The amount of aniline incorporated in this step was selected in order to cover the SBA-15 surface with an aniline monolayer ³¹. Approximately 0.5 g of the SBA-15 hard template was added to ±200 mL of the 0.5 M HCl aqueous solution and stirred for 15 minutes. Afterwards, the appropriate amount of aniline, calculated from the mass and specific surface area (S_{BET}) of the SBA-15 hard template and cross-sectional area (43 Å²) and density (1.02 g cm⁻³) of aniline, was added and the whole mixture was stirred for 1 h in an ice bath. Finally, a 1.2 molar excess of the radical initiator, ammonium peroxydisulfate (APS), dissolved in ±50 mL of the 0.5 M HCl aqueous solution, was added and the mixture was stirred for 24 h in an ice bath. Afterwards, the solvent was removed in a rotary evaporator and the sample was dried in an oven at 100 °C. The sample was then placed into the tubular furnace where it underwent a pyrolysis for 3 h at 900 °C (3.3 °C min⁻¹) under constant Argon (Ar) flow (1 cm³ s⁻¹). In the second step of the synthesis, the remaining pore volume of the SBA-15 was loaded with carbon. The required amount of 2,3-dihydroxynaphthalene (2,3-DHN) was calculated using the remaining pore volume of the SBA-15 hard template and the density of 2,3-DHN (1.33 g cm⁻³). The, as obtained grey solid, from the first step was mixed with the appropriate amount of 2,3-DHN in acetone, and was allowed to stir at room temperature for 24 h. After evaporation of the solvent, the composite material was thermally treated for 2 h at 300 °C (3.3 °C min⁻¹) under a continuous Ar flow (1 cm³ s⁻¹), before washing the sample with acetone 3 times, collecting it by filtration and drying it overnight. A final

pyrolysis was then performed at 900 °C (3.3 °C min⁻¹) for 5 h under an Ar atmosphere (1 cm³/s). Finally, the silica template was removed by suspending the as obtained black solid in a 2M sodium hydroxide aqueous solution while stirring for 8 h at 100 °C under reflux. The SnO₂-N-OMC material was collected in the form of a black solid by filtration and was dried at 100 °C^{31,32}.

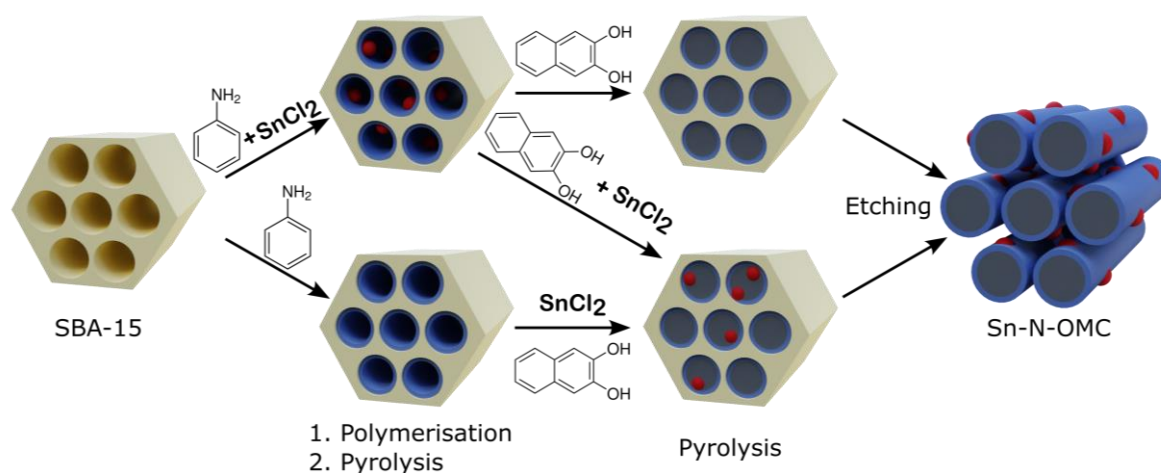


Figure 1. Synthesis method SnO₂ nitrogen-doped ordered mesoporous carbon electrocatalysts

Table 1. Detailed overview (SnO₂-)N-OMC Syntheses

Catalyst	Hard Template	Aniline (mL)	APS (g)	2,3-DHN (g)	SnCl ₂ .2H ₂ O (g)	Step
N-OMC (1)	SBA-15 (1)	0.182	0.5454	0.7000	0	/
SnO ₂ -N-OMC (1)	SBA-15 (2)	0.185	0.5557	0.6982	0	Aniline
SnO ₂ -N-OMC (2)	SBA-15 (3)	0.179	0.5364	0.6491	0.1	2,3-DHN
SnO ₂ -N-OMC (3)	SBA-15 (4)	0.182	0.5454	0.6366	0.4	Aniline
SnO ₂ -N-OMC (4)	SBA-15 (5)	0.221	0.6618	0.7788	0	2,3-DHN
SnO ₂ -N-OMC (5)	SBA-15 (6)	0.179	0.5374	0.6778	0.1	Aniline
SnO ₂ -N-OMC (6)	SBA-15 (7)	0.168	0.5035	0.6323	0.3	2,3-DHN
					0.2	Aniline
					0.2	2,3-DHN

2.3 Physicochemical Characterization

Nitrogen physisorption was performed at 77 K, utilizing a Quantachrome Quadrasorb SI (Quantachrome Instruments, Boynton Beach, FL, USA) automated surface area & pore size analyzer.

Prior to all N₂ physisorption measurements, all samples were degassed at 200 °C for 16 h. The specific surface area (S_{BET}) was calculated using the Brunauer-Emmet-Teller (BET) equation and Quantachrome QuadraWin software. **X-ray Powder Diffraction (XRD)** was evaluated using a Bruker D8 ECO powder diffractometer with a LYNXEYE XE-T detector and Cu K-Alpha radiation. SBA-15 samples were probed from 0.5 – 20° 2 θ , while all (Sn) N-OMC samples were measured from 20 – 80° 2 θ and compared with the crystallography open database (COD) #1534785 for tetragonal SnO₂. **Raman spectroscopy** was performed using a Micro-Raman Horiba (Xplora Plus Microscope) equipped with a 532 nm green laser. Raman spectra were recorded from 750 – 2000 cm⁻¹ Raman shift in order to investigate the degree of graphitization. All samples were measured, coated on a glass slide to avoid interference of the carbon based gas diffusion electrode. **X-ray Photoelectron Spectroscopy (XPS)** was performed on a PHI-VersaProbe III, equipped with an Al K α (1486.6 eV) monochromatic X-ray source. An area of \varnothing 100 μm was measured, using a pass energy of 26 eV for the high-resolution (HR) spectra and an automatic neutralizer. The wt% is calculated from the atomic concentrations, based on internal standards in the PHI MultiPak software. The high resolution C1s, O1s, N1s and Sn3d5 XPS spectra were processed using the PHI MultiPak software. **Inductively Coupled Plasma Optical Emission Spectroscopy (ICP-OES)** was performed on a PerkinElmer Optima 8300 after digestion of the samples in a Milestone Ethos UP microwave digestion system. All (SnO₂-)N-OMC samples were analyzed in two-fold. To this extent, 10 mg of each sample was weighed out in a Teflon microwave vessel after which 2 mL of H₂O₂, 8 mL of HNO₃ and 3 mL of HF were added to each vessel. The vessels were left overnight and underwent microwave digestion the following day. After the first digestion, an additional 1 mL of H₂O₂ and 2 mL of HF were added and the microwave digestion was repeated a second time. Finally, 2 mL of HNO₃ and 1 mL of H₂O₂ were added for a third microwave digestion and the digested content of the vessels was transferred and diluted to 50 mL. Before the ICP-OES analysis, the samples were diluted 10 times with 5% HNO₃. A blank sample of acids and a calibration series ranging from 5 ppb to 10 ppm of tin and multi-element standards were used for analysis. **High Angle Annular Dark-Field Scanning Transmission Electron Microscopy (HAADF-STEM)** as well as **Energy Dispersive X-ray Spectroscopy (EDS)** was performed using an aberration-corrected cubed ThermoFisher Scientific Titan transmission electron microscope operating at 200 kV, equipped with the ChemiSTEM system³⁴. HAADF-STEM was performed *ex situ* after the electrochemical measurements, by scraping the samples off of the GDE, suspending them in ethanol and dropcasting them on Ultra Thin Film (UTF) carbon-coated Cu TEM grids. The **CO₂ adsorption capacity** was determined by means of **TGA**, using a NETZSCH STA 449 F3 Jupiter with a rhodium furnace. Prior to the measurements, all samples were pretreated under an inert nitrogen atmosphere to desorb all adsorbed species. Afterwards, CO₂ was allowed to adsorb onto the samples by keeping them isothermal at 30°C for 4 hours under a 100 sccm N₂ and 33 sccm

CO₂ flow. Finally, the samples were reheated to 200°C at a rate of 10 °C min⁻¹ under 100 sccm N₂, remaining isothermal at 200°C for 2 hours under 100 sccm N₂ to allow all CO₂ to be desorbed before being cooled down to 30°C under an inert N₂ atmosphere.

2.4 Electrochemical Measurements

2.4.1 Uncompensated Resistance Determination

The **uncompensated resistance R_u (Ohmic drop)**, was determined by means of a current interrupt measurement, prior to the electrochemical CO₂ reduction experiments. A potential of -4 V vs. Ag/AgCl was applied before triggering the current interrupt circuit and measuring the potential decay over a time period of 2 ms. The uncompensated resistance was obtained from a linear regression between 0 s and 500 μ s in the Metrohm Autolab Nova 2.1.5 Software, and was consistently between 7 to 10 Ω for all measurements. The utilized Ag/AgCl reference electrode is regularly checked versus our ground Ag/AgCl reference electrode. All reported potentials were corrected for this resistance after measurement and converted to the RHE scale.

2.4.2 Electrochemical CO₂ Reduction

Gas diffusion electrodes (GDEs) are prepared by spray coating a 25 cm² Sigracet 39 BB GDE with an ink made from the synthesized electrocatalyst powders. For deposition with a target electrocatalyst loading of 1.5 ± 0.1 mg cm⁻², the ink consists of 75 mg of the as-synthesized (SnO₂-)N-OMC electrocatalyst, and 0.375 g of a 5 wt% Nafion solution in approximately 10 mL of a 1:1 Milli-Q (18.2 M Ω -cm @ 25 °C):IPA solution. Afterwards, the GDE is divided into 6 smaller GDEs, which are used as cathodes in a small flow-by electrolyzer with a geometric electrochemically active surface area of 1 cm². The flow-by electrolyzer consists out of two backplates, PMMA insulators, copper current collectors, a graphite cathodic compartment and an adjacent PMMA catholyte flow field with reference electrode, a graphite anodic compartment and several gaskets for appropriate sealing of the electrolyzer. A full schematic representation of the utilized flow-by electrolyzer and setup is provided in the supporting information (Figure S1).

Electrocatalytic CO₂ reduction experiments of both 1 and 24 hours were conducted by applying a current density of -100 mA cm⁻² to the aforementioned flow-by electrolyzer. The 0.5 M KHCO₃ catholyte is fed single pass at a flow rate of 2 mL min⁻¹, while the 2 M KOH anolyte is recycled at an equal flow rate. Pure CO₂ is fed through the backside of the GDE at a flow rate of 15 mL min⁻¹, which was determined to be the ideal flow rate to achieve the highest FE% for the eCO₂R. A Ni foam is used as counter electrode (anode), and a Nafion 117 membrane and Ag/AgCl reference electrode were used. Liquid samples were taken, for a period of 2 minutes, after 15 minutes and after 1 hour to

determine the FE% towards formate by means of HPLC. Gaseous products were detected by means of in-line GC. For the long-term 24 h electrolysis experiments, additional samples were taken during the first 6 hours of the reaction and once again after 24 h. The reported data was reproduced and an average value is reported for all FE_{FA} and iR-compensated potentials.

3. Results and Discussion

3.1 Physicochemical Characterization

Similar to the SBA-15 hard template (physicochemical characterization in SI, Figure S2 and S5A, B), N-OMC materials are known to have a well ordered, high specific surface area^{31,32}. The effect of incorporating SnO₂ species during the synthesis on the specific surface area and structure of the N-OMC support material was investigated by nitrogen physisorption, utilizing the BET equation. The adsorption-desorption isotherms of all (SnO₂-)N-OMCs, as depicted in Figure 2, are classified as a composite Type IVa + Type II isotherm with a clear hysteresis.

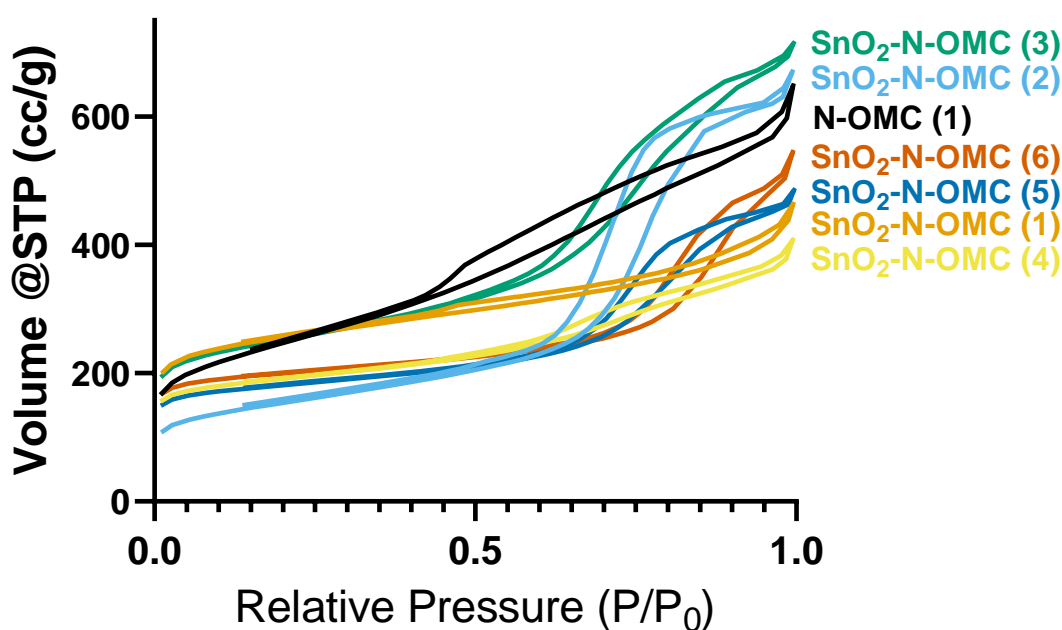


Figure 2. Nitrogen adsorption-desorption isotherms (SnO₂-)N-OMC electrocatalysts

Type IVa isotherms are indicative of mesoporous adsorbents and typically end in a final, nearly horizontal, saturation plateau near $P/P_0 = 1$. Type II isotherms, on the other hand, are characterized by the unrestricted monolayer-multilayer adsorption on nonporous or macroporous adsorbents, resulting in the absence of a plateau near $P/P_0 = 1$. Given that the adsorbed amount appears to increase infinitely when $P/P_0 = 1$, indicating either interparticle adsorption or the presence of macropores, but

hysteresis does manifest, pointing towards mesopores, all samples were classified as a composite Type IVa + Type II isotherm. According to the recommendation in the IUPAC technical report, the total pore volume of such a composite Type IVa + Type II isotherm cannot accurately be evaluated since the isotherm is not horizontal near $P/P_0 = 1$. Nevertheless, the pore volume was derived from the adsorbed amount close to unity (i.e. $P/P_0 \approx 0.95$) by means of the Barrett, Joyner and Halenda (BJH) method for an indication³⁵. The specific surface areas and corresponding pore volumes and sizes are summarized in Table 2. The BET surface area and pore size distribution plots are provided in the supporting information (Fig. S3).

Based on the adsorption-desorption isotherms, SnO₂-N-OMC (1) and SnO₂-N-OMC (4) appear to be the only two samples with a less neatly ordered mesoporous structure, though they still have high specific surface areas, as their isotherms have a higher resemblance to a Type II isotherm for nonporous or macroporous materials. Nonetheless, both SnO₂-N-OMC (1) and SnO₂-N-OMC (4) isotherms contain hysteresis, indicating the presence of cylindrical (meso)pores, larger than ~ 4 nm³⁵. Interestingly, these are the only two SnO₂-N-OMC samples where the entirety of the SnCl₂ precursor was added simultaneously with the 2,3-dihydroxynaphthalene. All other SnO₂-N-OMC adsorption-desorption isotherms have a closer resemblance to a Type IVa isotherm, indicating well-ordered mesoporous materials. These observations seem to imply that it's important to at least add a part of the SnCl₂ precursor with the aniline and that adding the entire SnCl₂ precursor during the 2,3-DHN step appears to hinder the formation of a neatly ordered mesoporous carbon structure. Low angle XRD of the resulting (SnO₂)-N-OMC electrocatalysts (Fig. S4), however, only weakly indicates a neatly ordered mesoporous structure for some of the supporting N-OMC materials. Nevertheless, with the nitrogen adsorption-desorption isotherms and visual confirmation, obtained via electron microscopy (Fig. S5), we can confirm that all SnO₂-N-OMC electrocatalysts possess areas which are neatly ordered and others that are amorphous due to the incorporation of the SnCl₂ precursor during the synthesis.

For Type II and Type IVa isotherms, the linearity of the BET plot is limited to a part of the isotherm, most commonly in the relative pressure range of $\sim 0.05 - 0.30$. However, for our SnO₂-N-OMC materials, this BET range is shifted towards lower relative pressures due to the high adsorption energy of the nitrogen on the graphitized carbon³⁵.

Table 2. Morphological properties of the (SnO₂)-N-OMC electrocatalysts

Catalyst	S _{BET} (m ² g ⁻¹)	Pore volume (cm ³ g ⁻¹)*	Pore size (nm)**
N-OMC (1)	856	0.88	-
SnO ₂ -N-OMC (1)	952	0.63	-
SnO ₂ -N-OMC (2)	547	0.96	7.0
SnO ₂ -N-OMC (3)	925	1.05	4.5
SnO ₂ -N-OMC (4)	722	0.56	-
SnO ₂ -N-OMC (5)	689	0.70	4.1
SnO ₂ -N-OMC (6)	767	0.74	3.9

* The pore volume was derived from the adsorbed amount close to unity (i.e. $P/P_0 \approx 0.95$) by means of the Barrett, Joyner and Halenda (BJH) method to get an indication since it is conventionally not determined for composite Type IVa + Type II isotherms.

**Not all pore sizes could be determined using the BJH method because of the composite Type IVa + Type II isotherms.

The as-synthesized SnO₂-N-OMC materials have a varying surface area, pore volume and pore size. Here, it is again apparent that both the SnO₂-N-OMC (1) and SnO₂-N-OMC (4) electrocatalysts have a less neatly ordered mesoporous structure with the lowest pore volumes. Nevertheless, according to these physisorption results, all SnO₂-N-OMC electrocatalysts possess a high surface area (> 500 m² g⁻¹) and a high volume of (meso)pores, which is promising for their role as CO₂ capturing agents. This variety in S_{BET}, which is (partially) inherent to the SnO₂-N-OMC synthesis, allows us to explore the influence of the N-OMC support material on the electrochemical performance of the SnO₂ species for the eCO₂R towards formate.

Information related to the degree of graphitization (i.e. the ratio of the areas of the D and G bands) and knowledge concerning the crystalline structure, chemical nature and space group symmetry were obtained by Raman spectroscopy and XRD, respectively. The normalized Raman spectra (Figure 3) display two broad peaks at 1350 cm⁻¹ and 1600 cm⁻¹, the former usually referred to as the D-band, originating from edge defects of the graphitic domain, and the latter identified as the G-band, which is assigned to planar vibration of sp² carbon atoms in an ideal graphitic layer^{31,36,37}. Since the ratio of the areas of the D and G bands (I_D/I_G), which is inversely proportional to the degree of graphitization, is > 1 and comparable for all samples, we can conclude that all SnO₂-N-OMC electrocatalysts have a clear graphitic character, despite amorphous segments. The addition of an SnO₂ precursor during the N-OMC synthesis had no major influence on the resulting degree of graphitization of the N-OMC³¹.

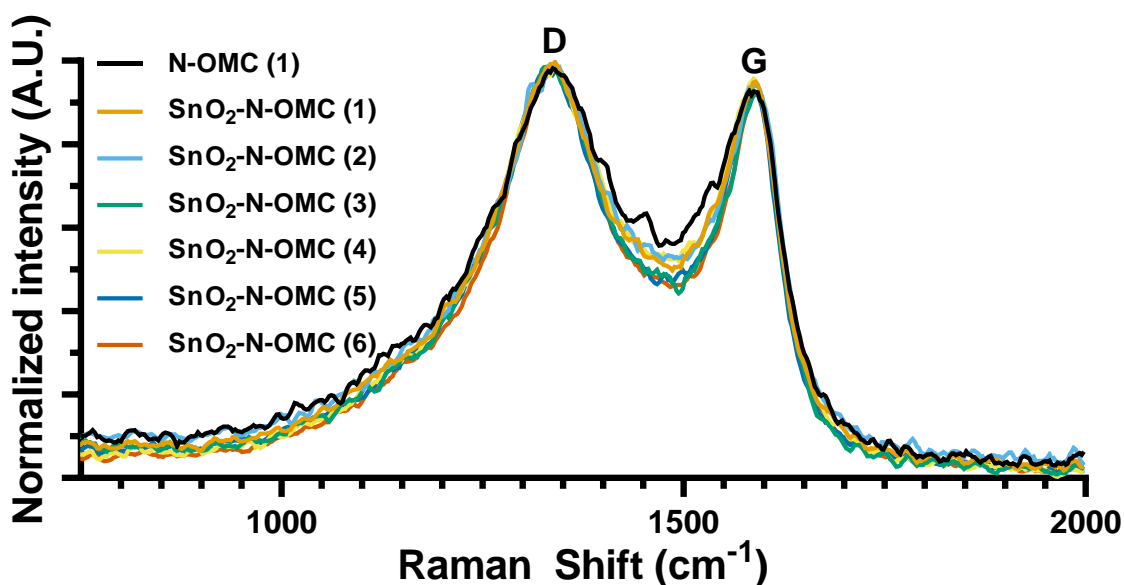


Figure 3. Normalized Raman spectra of the as-synthesized (SnO₂)-N-OMC electrocatalysts, recorded between 750 and 2000 cm⁻¹ with a 532 nm green laser

The wide angle diffractograms (Figure 4) display the typical diffraction pattern with peaks at $2\theta = 26.5^\circ$, 33.8° , 37.9° , 38.9° , 42.6° , 51.7° , 54.7° , 57.7° , 61.8° , 64.6° , 65.8° , 71.1° and 78.5° , present in all SnO₂-N-OMC samples. These peaks are attributed to reflections of the (110), (101), (200), (111), (120), (211), (220), (002), (130), (112), (301), (202) and (321) planes, respectively, of tetragonal SnO₂ (COD #1534785)^{38,39}. Additionally, two broad and weak peaks are observed in the N-OMC diffractogram at approximately 25° and 43.5° 2θ , which correlate to amorphous carbon and are also observed in the diffractograms of the SnO₂-N-OMC catalysts⁴⁰. Again, no distinctive differences are observed in terms of the crystalline structure and chemical nature of the SnO₂ species, which are all confirmed to be tetragonal SnO₂. This allows for differences in the electrochemical performance to be attributed solely to the morphology of the SnO₂ species, SnO₂ loading and influences of the N-OMC support material.

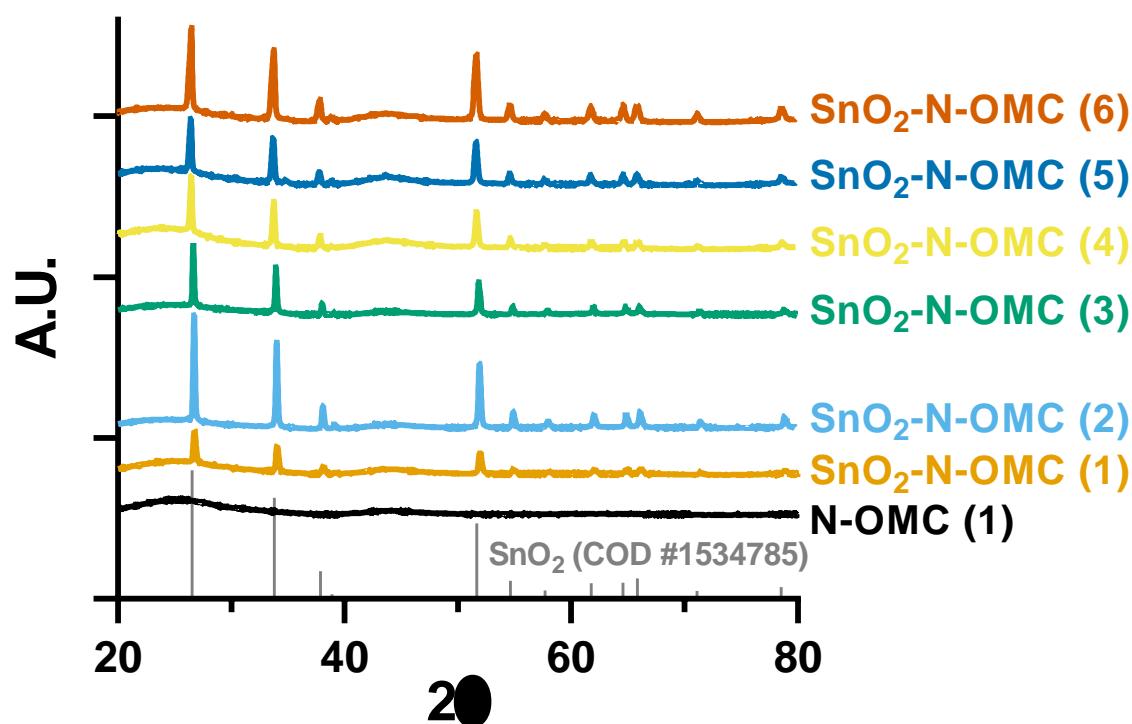


Figure 4. Wide angle X-ray diffractogram of the as-synthesized $(\text{SnO}_2)\text{-N-OMC}$ catalysts, compared with the Crystallography Open Database (COD) #1534785 for tetragonal SnO_2 .

3.2 Electrochemical CO_2 Reduction

The electrochemical performance of the $(\text{SnO}_2)\text{-N-OMC}$ electrocatalysts was investigated in a small flow-by electrolyzer with a geometric surface area of 1 cm^2 (Figure S1). By performing a 1 h chronopotentiometric experiment at a constant applied current density of 100 mA cm^{-2} , the average iR-compensated cathodic operating potential (Figure 5a) and FE_{FA} (Figure 5b) were determined. The overall average FE% for all seven electrocatalysts has been provided in the SI (Fig. S6), showing no other detectable products being formed other than formate, hydrogen and carbon monoxide. Furthermore, it approaches a total FE (%) of approximately 100% when taking into account the inherent error margins of all separately reported Faradaic Efficiencies.

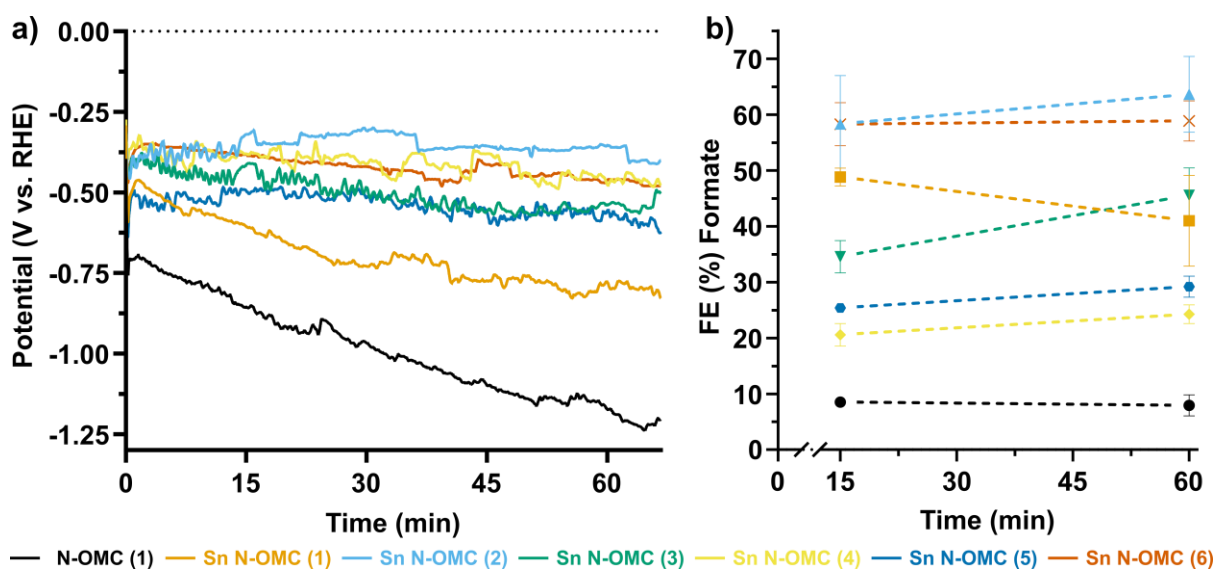


Figure 5. a) average *iR*-compensated potential (V vs. RHE) and b) average FE% towards formate with error bars, plotted as a function of time at a constant current density of 100 mA cm^{-2} for 1 h.

Several trends are observed when looking at the electrocatalytic performance and Faradaic Efficiency towards FA of the $(\text{SnO}_2)\text{-N-OMCs}$. First, the pristine nitrogen doped ordered mesoporous carbon material (N-OMC (1)) has a low average FE_{FA} of 8% and a continuously increasing cathodic potential over the course of 1 h, indicating that, on its own, it is not suited for the electrochemical reduction of CO_2 to formate. Interestingly, this trend of an increasing cathodic potential appears to diminish by combining the N-OMC with SnO_2 species, as evidenced by the potential-time curves of the $\text{SnO}_2\text{-N-OMC}$ electrocatalysts. $\text{SnO}_2\text{-N-OMC}$ (1) has the lowest amount of SnO_2 and already exhibits a significantly smaller slope. Moreover, upon further increasing the SnO_2 content, a constant cathodic potential is achieved. Therefore, this continuously increasing cathodic potential is hypothesized to originate from the blocking of active sites due to inefficient conversion of adsorbed CO_2 by the N-OMC or the competing HER which increases the local pH, resulting in fewer protons and an increasing potential to maintain a constant current at low FE_{FA} .

Additional measurements of the most stable and best performing $\text{SnO}_2\text{-N-OMC}$ (2) electrocatalyst, with varying CO_2 and N_2 mixed flows (Figure S7), revealed a stable uncompensated potential for both the eCO_2R (100/0, CO_2/N_2) and HER (0/100, CO_2/N_2). When forcing a combination of the eCO_2R and HER (50/50, CO_2/N_2), however, the FE_{FA} drops to approximately 35% and a similar continuously increasing cathodic potential is observed.

Furthermore, the CO_2 adsorption capacity of the pristine N-OMC (1), best performing $\text{SnO}_2\text{-N-OMC}$ (2) and worst performing $\text{SnO}_2\text{-N-OMC}$ (4) electrocatalysts were determined by means of TGA and compared to the equally porous, non-nitrogen doped, commercially available Ensaco[®] carbon black ($S_{\text{BET}} 770 \text{ m}^2 \text{ g}^{-1}$). With $0.291 \text{ mmol g}^{-1}$, the Ensaco[®] carbon black adsorbed the lowest amount of CO_2 ,

while the pristine N-OMC (1) is able to adsorb approximately 2.5 times the amount of CO₂ (0.725 mmol g⁻¹). Both SnO₂-N-OMC electrocatalysts adsorbed 0.710 mmol g⁻¹ and 0.834 mmol g⁻¹ for SnO₂-N-OMC (2) and SnO₂-N-OMC (4), respectively. Normalized to their specific surface area (S_{BET}), Ensaco[®] carbon black and the pristine N-OMC (1) adsorbed 0.378 μmol m⁻² and 0.847 μmol m⁻², respectively, verifying the previously hypothesised increased CO₂ adsorption by incorporating nitrogen into the supporting carbon material. Furthermore, the best performing SnO₂-N-OMC (2) adsorbed more CO₂ (1.299 μmol m⁻²) than SnO₂-N-OMC (4) (1.155 μmol m⁻²), revealing that by incorporating SnO₂ species, the CO₂ adsorption capacity is increased even further.

Combining these results indicates that, while both hypotheses contribute to the continuously increasing cathodic potential, for the SnO₂ containing N-OMC electrocatalysts, the latter hypothesis is the most predominant cause. The continuously increasing cathodic potential for N-OMC (1), under continuous CO₂ flow, however, is dominated by the blocking of active sites (for the HER) due to inefficient conversion of the adsorbed CO₂.

The addition of SnO₂ species boosts the electrocatalytic selectivity towards formate from 8% for the blank N-OMC (1) to 59% and 61% for the SnO₂-N-OMC (6) and SnO₂-N-OMC (2) electrocatalysts, respectively, approaching the state-of-the-art of comparable materials (Table S1). The combination of high current densities and low overpotentials with a selectivity of around 60% puts our materials at the same level or above the state-of-the-art in the field. The SnO₂ species are thus far more active for the eCO₂R towards FA and appear to predominantly determine the electrochemical performance, suppressing the electrochemical behavior of the N-OMC which was initially expressed by the continuously decreasing potential and a low selectivity towards formate. Finally, a latency effect is noticed in the FE_{FA} of most SnO₂-N-OMC electrocatalysts, presumably caused by the longer formate diffusion times, away from the active SnO₂ sites, through the mesoporous N-OMC supporting material

41.

Table 3. Composition of the (SnO₂)-N-OMC electrocatalysts in wt%, as determined by a) ICP-OES and b) XPS

Catalyst	Sn ^a (wt%)	Sn ^b (wt%)	C ^b (wt%)	N ^b (wt%)	O ^b (wt%)
N-OMC (1)	0.08	0.00	90.27	2.06	7.67
SnO ₂ -N-OMC (1)	0.27	-	-	-	-
SnO ₂ -N-OMC (2)	1.15	2.47	90.91	0.32	6.30
SnO ₂ -N-OMC (3)	0.55	-	-	-	-
SnO ₂ -N-OMC (4)	0.69	3.33	87.79	0.98	7.90
SnO ₂ -N-OMC (5)	1.01	-	-	-	-
SnO ₂ -N-OMC (6)	0.57	4.44	86.00	0.22	9.34

In terms of selectivity, a wide variety, ranging from an average 22% for SnO₂-N-OMC (4) to 61% for SnO₂-N-OMC (2), was obtained by incorporating equal amounts of SnO₂ precursor during different steps of the N-OMC synthesis. ICP-OES and XPS analysis (Table 3 and Figure S8), however, revealed that while equal amounts of Sn precursor were added in most of the syntheses, most of the Sn wasn't retained in the final material, providing a widely varying amount of SnO₂ that was actually included. Moreover, upon comparing the Sn content, as determined by ICP-OES and XPS, it becomes clear that most of the Sn is present on the surface of the SnO₂-N-OMC electrocatalyst material and not incorporated inside the mesoporous carbon structure. Low and high magnification HAADF-STEM imaging combined with EDS elemental mapping confirmed the presence of a wide variety of SnO₂ species, ranging from large irregular SnO₂ species to differently sized SnO₂ nanoparticles, as depicted in figure S9, all of them having the rutile tetragonal SnO₂ structure (space group: P4₂/mnm). These SnO₂ species are mostly found at the outer part of the mesoporous carbon support. In addition, crystalline and non-crystalline atomic clusters, which have a significantly higher contrast compared to their background in high resolution HAADF-STEM images, lay among the N-OMC matrix. EDS elemental mapping of these clusters only showed carbon and silicon signals from the N-OMC, without a clear presence of Sn. This spectroscopy based result can be attributed to the small size of these clusters and their sensitivity under the electron beam, which only allowed us to use very short acquisition times. However, the analysis of the high resolution data of these crystalline clusters (Figure S9B) confirms that, similar to the bigger SnO₂ species (Figure S9C, F),²⁹ the interatomic distances are in agreement with the d-spacings of rutile SnO₂, a strong indication that they are Sn-based.

SnO₂-N-OMC (2) and SnO₂-N-OMC (6), respectively, enclose considerably larger irregular SnO₂ species and differently sized SnO₂ nanoparticles, than the least performing electrocatalyst, SnO₂-N-OMC (4). Considering that Zhao *et al.* reported atomically dispersed Sn species to promote the eCO₂R towards

CO and Sn nanoparticles are more selective towards formate, it is obvious that the large irregular SnO₂ species and/or the SnO₂ nanoparticles of different sizes are crucial and dominate the electrochemical performance of the SnO₂-N-OMC electrocatalysts when formate is the target product²⁹. The moderate electrochemical performance of the other three SnO₂-N-OMC electrocatalysts (1, 3 and 5) highlights that the morphology of the SnO₂ species appears to be more important than the SnO₂ loading. Nonetheless, these SnO₂-N-OMC electrocatalysts seemingly have less selective SnO₂ species, compared to the best performing SnO₂-N-OMCs, resulting in a lower selectivity towards FA.

In summary, the observed electrochemical performance of the SnO₂-N-OMC electrocatalysts is a result of the combined behavior of the N-OMC (S_{BET} surface area, N-dopant, conductivity, etc.) support and the different SnO₂ species. As demonstrated, the N-OMC material independently isn't suited for the selective eCO₂R towards FA, which is why the SnO₂ species make the largest contribution to the electrochemical performance (especially selectivity) of the SnO₂-N-OMC electrocatalysts. Furthermore, the enhanced CO₂ adsorption, due to the N-OMC support material appears to positively influence the overpotential, in comparison to the state-of-the-art (Table S1). As a result, all SnO₂-N-OMC electrocatalysts demand a lower overpotential for the conversion of CO₂ towards FA at the industrially relevant current density of 100 mA cm⁻². The N-OMC support material itself, requires the largest overpotential, as depicted in Figure 5a, presumably caused by the poor conversion of the more easily adsorbed CO₂. However, we've demonstrated that we are able to significantly increase the FE_{FA} and lower the overpotential, utilizing a minimal amount of SnO₂ species, with the most selective morphologies being large irregular SnO₂ species and heterogeneous SnO₂ nanoparticles. An optimal combination of both SnO₂ species and the N-OMC carbon capture medium could thus result in a synergistic effect for the eCO₂R towards FA.

The long-term electrocatalytic performance and degradation pathways of the two best performing electrocatalysts (SnO₂-N-OMC (2) and SnO₂-N-OMC (6)) were evaluated by performing a 24 h chronopotentiometric experiment at an applied current density of 100 mA cm⁻², combined with *ex situ* HAADF-STEM imaging. After starting at a similar FE_{FA} of approximately 60%, the SnO₂-N-OMC (2) and SnO₂-N-OMC (6) electrocatalysts started to display a difference in stability after only 2 h of electrolysis at 100 mA cm⁻², as depicted in Figure 6. The FE_{FA} of SnO₂-N-OMC (2) increases to an average of 64% over the course of the first 6 hours, while the selectivity of the SnO₂-N-OMC (6) decreases to 28% after 6 h and even further to 12% at -0.95 V vs. RHE after 24 h. Eventually, after 24 h of operation, the FE_{FA} of SnO₂-N-OMC (2) decreases to an average of 43% at an operating potential of -0.60 V vs. RHE. *Ex situ* HAADF-STEM imaging of both electrocatalysts after 24 h of electrolysis (Figure 7A, B) reveals the morphological degradation of the large SnO₂ species, which are pulverized and agglomerated, similar

to the deterioration reported by Wu *et al.*⁴² and described in our previous publication concerning pomegranate-structured SnO₂@C electrocatalysts⁴³.

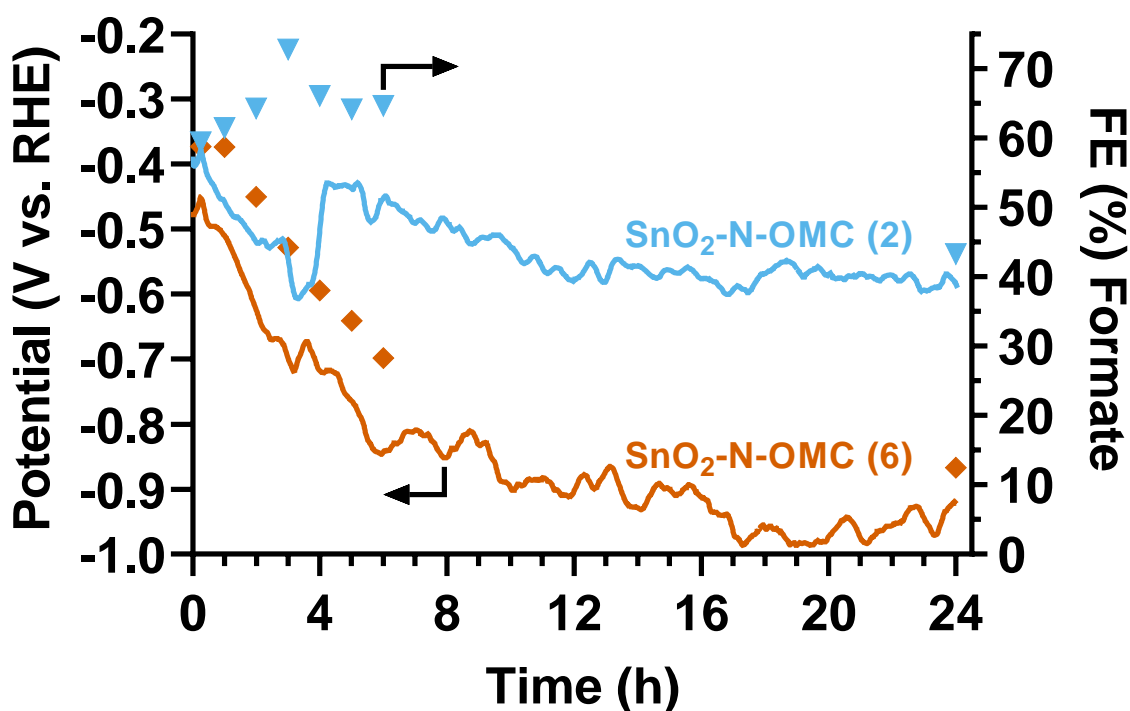


Figure 6. average *iR*-compensated potential (V vs. RHE) and FE% towards formate of the SnO₂-N-OMC (2) and SnO₂-N-OMC (6) electrocatalysts, plotted as a function of time at a constant current density of 100 mA cm⁻² for 24 h.

This dissimilar electrocatalytic performance can be ascribed to a combination of morphological (pulverization and agglomeration) and chemical (*in situ* SnO₂ reduction towards metallic Sn) deterioration. Similar to the previously reported pomegranate-structure SnO₂ electrocatalyst, the loss of selectivity of the SnO₂-N-OMC (2) electrocatalysts due to the *in situ* SnO₂ reduction, is temporarily offset by the pulverization providing additional SnO₂ active sites for the eCO₂R towards FA. In the case of SnO₂-N-OMC (6), the initial SnO₂ species were already significantly smaller than the ones present in SnO₂-N-OMC (2), leading towards less pulverization (and more agglomeration) and consequently to less fresh SnO₂ sites being formed to offset the *in situ* SnO₂ reduction and more rapid loss in selectivity as a result (Figure 6).

This was further confirmed by postmortem *ex situ* XRD (Figure S10), which shows a decrease in the intensity of the diffraction pattern for tetragonal SnO₂ (COD #1534785) at the expense of an increase in the intensity of metallic Sn (COD #9008570)⁴⁴. Furthermore, the appearance of additional peaks is observed, which can be attributed to KHCO₃ (COD #9016304) as a result of salt deposition during the eCO₂R⁴⁵. This *in situ* SnO₂ reduction to metallic Sn (space group: I4₁/amd), observed by *ex situ* XRD and HAADF-STEM imaging and the corresponding Fourier Transform pattern, combined with

quantified (for atomic %) EDS elemental mapping (Figure 7C, D) in both SnO₂-N-OMC electrocatalysts after 24 h of electrolysis, is determined to be the most detrimental degradation pathway, resulting in the direct loss of selectivity. While morphological stability of the Sn-based electrocatalyst is important in the long run, chemical stability to withstand *in situ* SnO₂ reduction appears to be more crucial as this directly correlates to a severe loss in selectivity.

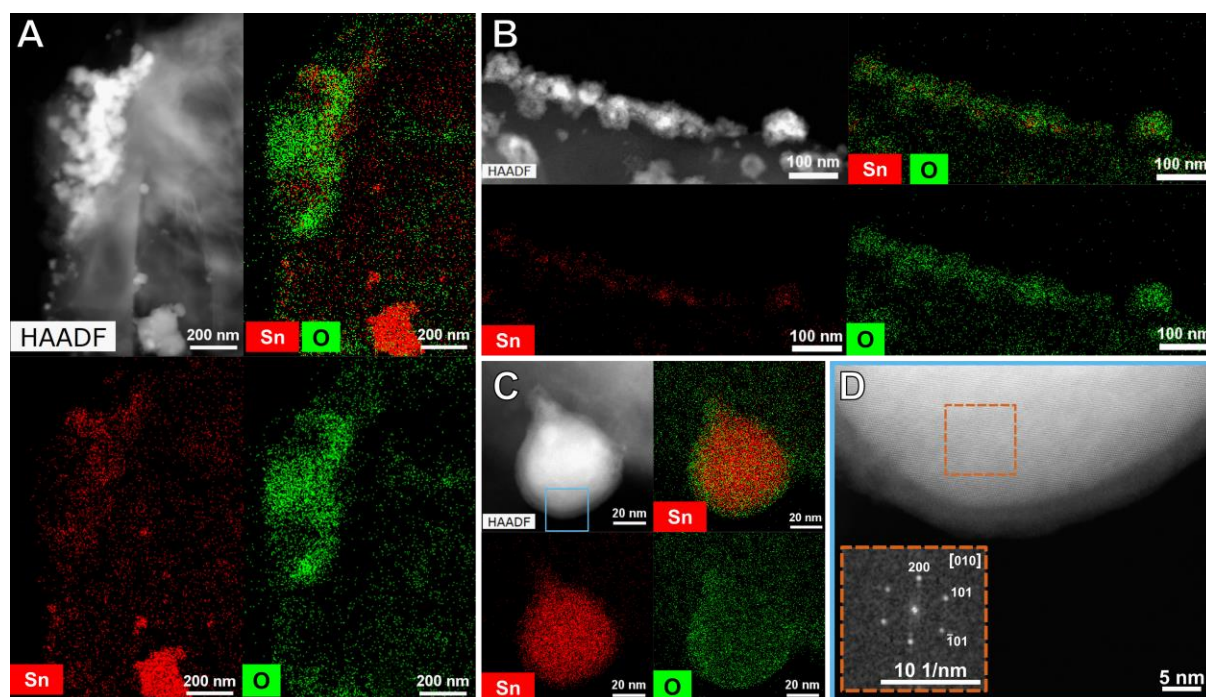


Figure 7. HAADF-STEM images and EDS elemental maps quantified for atomic % of A) SnO₂-N-OMC (2), B) SnO₂-N-OMC (6) after 24 h of electrolysis at 100 mA cm⁻² and C, D) HAADF-STEM images with the corresponding FT pattern and EDS elemental maps quantified for atomic % of a partially re-oxidized *in situ* reduced Sn nanoparticle in SnO₂-N-OMC (2).

To date, no universal consensus concerning the active site of SnO₂-based electrocatalysts and the reaction mechanism for the eCO₂R towards formic acid has been reached in state-of-the-art literature. Nonetheless, it is obvious that oxides play an important role in their electrocatalytic performance. In literature, multiple reports have been made concerning the importance of oxides and their dynamic nature during the eCO₂R. For example, Cheng *et al.*⁴⁶ described the nature of the active sites of OD-Cu electrocatalysts for the eCO₂R, while Bagchi *et al.*⁴⁷ reported on the time- and potential-dependent dynamic nature of an OD-PdIn nano-electrocatalyst. Similar observations concerning the dynamic and potential dependent nature of Sn oxides have been made for SnO₂-based electrocatalysts. Therefore, as evidenced here, we believe that after the improved initial adsorption of CO₂, due to the incorporation of nitrogen, the formation of surface-bound Sn carbonate is a key chemical intermediate in the eCO₂R towards FA on Sn-based electrodes⁴⁸. Bocarsly *et al.* argued that prior to the eCO₂R, the presence of surface SnO₂ species enables the formation of Sn²⁺ oxyhydroxide through proton reduction. Subsequent reaction with CO₂ results in the formation of a surface-bound carbonate, which

is converted to HCOO^- via a two-electron and one proton transfer. After desorption of the final product, the Sn-based electrocatalyst is returned to its Sn^{2+} oxyhydroxide state^{19,48}. This metastable Sn^{2+} oxyhydroxide has been proposed by multiple researchers as the active site for the eCO_2R towards FA on SnO_2 -based electrodes. Analysis of the most predominant degradation mechanisms in the SnO_2 -N-OMC electrocatalysts indeed confirms the importance of surface oxide species. It is important to note, however, that the proposed mechanism in figure 8 is the most plausible one, based on state-of-the-art literature, and that further experimental and theoretical studies, which fall out of the scope of this work, are required to confirm this. Previously, we proposed several mitigation strategies such as lowering the overpotential, co-electrolysis of CO_2 with low concentrations of oxygen (or other oxidants) or pulsed eCO_2R , to diminish the most detrimental degradation mechanism, the *in situ* SnO_2 reduction²⁶.

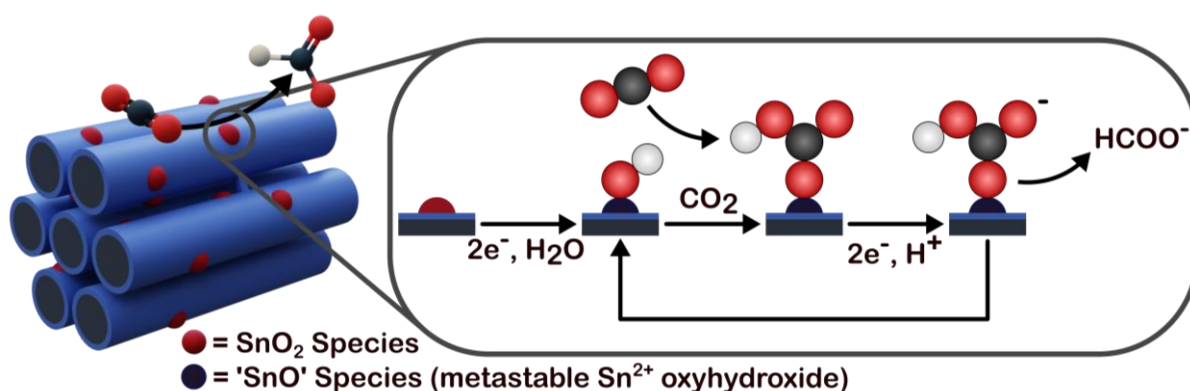


Figure 8. The most plausible reaction mechanism, based on state-of-the-art literature, for the eCO_2R towards formate on the SnO_2 -N-OMC electrocatalysts, with Sn^{2+} oxyhydroxide as metastable active site^{19,26,48}.

4. Conclusion

In conclusion, we have demonstrated that including SnO_2 during the N-OMC synthesis has no significant effect on the N-OMC morphology, as long as part of the SnO_2 precursor is added simultaneously with the aniline. Including a SnO_2 precursor during different stages of the N-OMC synthesis resulted in a wide variety of SnO_2 species, ranging from large irregular SnO_2 species to differently sized SnO_2 nanoparticles and Sn-based atomic clusters. More importantly, we've successfully demonstrated that we are able to significantly increase the FE_{FA} utilizing a minimal amount of SnO_2 , with the most selective morphologies being large irregular SnO_2 species and SnO_2 nanoparticles. Moreover, the SnO_2 -N-OMC electrocatalysts require a low overpotential, due to the enhanced CO_2 adsorption capacity of the N-OMC support, for the selective ($\pm 60\%$) conversion of CO_2 towards FA at the industrially relevant current density of 100 mA cm^{-2} , as such they perform better or at least as good as the current state-of-the-art. Finally, The long-term electrocatalytic stability and degradation pathways of the two best performing electrocatalysts (SnO_2 -N-OMC (2) and SnO_2 -N-OMC

(6)) were unraveled by combining 24 h chronopotentiometric experiments at an applied current density of 100 mA cm^{-2} with *ex situ* HAADF-STEM. While the FE_{FA} of $\text{SnO}_2\text{-N-OMC}$ (6) decreased from 59% to 12% over the course of 24 h, the $\text{SnO}_2\text{-N-OMC}$ (2) electrocatalyst displayed a smaller loss in FE_{FA} from 61% to 43%. This loss of selectivity was attributed to the *in situ* SnO_2 reduction, which in the case of the $\text{SnO}_2\text{-N-OMC}$ (2) is offset to a greater degree by the pulverization of large SnO_2 species, revealing 'fresh' and selective SnO_2 active sites for the eCO_2R towards FA. While morphological stability of the Sn-based electrocatalyst is important in the long run, chemical stability to withstand *in situ* SnO_2 reduction appears to be more crucial for future Sn-based electrocatalysts as this directly correlates to a severe loss in selectivity. Our exploration of the interplay between SnO_2 and the N-OMC carbon capture medium support material revealed that an optimal combination of both the SnO_2 species and the N-OMC carbon capture medium could thus result in a synergistic effect for the eCO_2R towards FA, especially when utilization of the N-OMC support material and incorporation of the SnO_2 species is optimized to morphologically stabilize the SnO_2 active species. Hence, future research concerning Sn-based electrocatalysts should focus on improving the morphological and chemical stability in order to yield industrially relevant Sn-based electrocatalysts for the eCO_2R towards FA.

Supporting Information

eCO_2R electrolyser setup, physicochemical characterization SBA-15, BET surface area and pore size distribution plots of all ($\text{SnO}_2\text{-}$)N-OMC electrocatalysts, low angle XRD, HAADF-STEM images, overall average $\text{FE}\%$, uncompensated potentials with varying CO_2/N_2 concentrations, state-of-the-art Sn-based and N-doped Sn-based electrocatalysts, XPS spectra and *ex-situ* wide angle XRD diffractograms of the as-synthesized $\text{SnO}_2\text{-N-OMC}$ electrocatalysts before and after 24h of eCO_2R .

Acknowledgements

K. Van Daele received financial support through a PhD fellowship strategic basic research (1S83320N) from the Research Foundation Flanders (FWO). Additionally, this project received funding in the framework of the Catalisti cluster SBO project CO2PERATE ("All renewable CCU based on formic acid integrated in an industrial micro-grid"), with financial support of VLAIO (Flemish Agency for Innovation and Entrepreneurship) (UA & VITO). Furthermore, this research was supported by the Interreg 2 Seas-program 2014-2020, co-funded by the European Regional Development Fund under subsidy contract No E2C 2S03-019 (UA & VITO). D.B. and D.P. acknowledge the support from European Union's Horizon 2020 MSCA-ITN programme under grant agreement No 955650 (CATCHY). S.H. is financially supported through a PhD fellowship strategic basic research (1S42623N) from the Research Foundation Flanders (FWO). R.J. received financial support of the federal Energy Transition Fund by FPS Economy. T.A.

acknowledges funding from the University of Antwerp Research fund (BOF). We acknowledge Prof. Tom Hauffman and Kitty Baert from the Electrochemical and Surface Engineering research group (SURF) at the VUB (Vrije Universiteit Brussel) for the X-ray Photoelectron Spectroscopy measurements. Prof. Christophe Vande Velde from the Intelligence in Processes, Advanced Catalysts and Solvents (iPRACS, UAntwerp) research group for the X-ray Powder Diffraction analysis. Prof. Pegie Cool, Prof. Vera Meynen and Radu-George Ciocarlan from the Laboratory of Adsorption and Catalysis (LADCA, UAntwerp) for the nitrogen physisorption and Raman spectroscopy measurements.

Conflicts of interest

There are no conflicts of interest to declare.

References

- (1) Mitchell, J. F. B. The “Greenhouse” Effect and Climate Change. *Rev. Geophys.* **1989**, *27* (1), 115–139.
- (2) Obama, B. The Irreversible Momentum of Clean Energy. *Science (1979)* **2017**, *355* (6321), 126–129.
- (3) Friedlingstein, P.; O’Sullivan, M.; Jones, M. W.; Andrew, R. M.; Gregor, L.; Hauck, J.; Le Quéré, C.; Luijkx, I. T.; Olsen, A.; Peters, G. P.; Peters, W.; Pongratz, J.; Schwingshackl, C.; Sitch, S.; Canadell, J. G.; Ciais, P.; Jackson, R. B.; Alin, S. R.; Alkama, R.; Arneeth, A.; Arora, V. K.; Bates, N. R.; Becker, M.; Bellouin, N.; Bittig, H. C.; Bopp, L.; Chevallier, F.; Chini, L. P.; Cronin, M.; Evans, W.; Falk, S.; Feely, R. A.; Gasser, T.; Gehlen, M.; Gkritzalis, T.; Gloege, L.; Grassi, G.; Gruber, N.; Gürses, Ö.; Harris, I.; Hefner, M.; Houghton, R. A.; Hurtt, G. C.; Iida, Y.; Ilyina, T.; Jain, A. K.; Jersild, A.; Kadono, K.; Kato, E.; Kennedy, D.; Klein Goldewijk, K.; Knauer, J.; Korsbakken, J. I.; Landschützer, P.; Lefèvre, N.; Lindsay, K.; Liu, J.; Liu, Z.; Marland, G.; Mayot, N.; McGrath, M. J.; Metzl, N.; Monacci, N. M.; Munro, D. R.; Nakaoka, S.-I.; Niwa, Y.; O’Brien, K.; Ono, T.; Palmer, P. I.; Pan, N.; Pierrot, D.; Pockock, K.; Poulter, B.; Resplandy, L.; Robertson, E.; Rödenbeck, C.; Rodriguez, C.; Rosan, T. M.; Schwinger, J.; Séférian, R.; Shutler, J. D.; Skjelvan, I.; Steinhoff, T.; Sun, Q.; Sutton, A. J.; Sweeney, C.; Takao, S.; Tanhua, T.; Tans, P. P.; Tian, X.; Tian, H.; Tilbrook, B.; Tsujino, H.; Tubiello, F.; van der Werf, G. R.; Walker, A. P.; Wanninkhof, R.; Whitehead, C.; Willstrand Wranne, A.; Wright, R.; Yuan, W.; Yue, C.; Yue, X.; Zaehle, S.; Zeng, J.; Zheng, B. Global Carbon Budget 2022. *Earth. Syst. Sci. Data* **2022**, *14* (11), 4811–4900.

- (4) Chen, S.; Liu, J.; Zhang, Q.; Teng, F.; McLellan, B. C. A Critical Review on Deployment Planning and Risk Analysis of Carbon Capture, Utilization, and Storage (CCUS) toward Carbon Neutrality. *Renewable Sustainable Energy Rev.* **2022**, *167* (December 2021), 112537.
- (5) Wang, T.; Park, A. H. A.; Shi, Y.; Gadikota, G. Carbon Dioxide Capture and Utilization - Closing the Carbon Cycle. *Energy Fuels* **2019**, *33* (3), 1693.
- (6) Wei, Y.-M.; Kang, J.-N.; Liu, L.-C.; Li, Q.; Wang, P.-T.; Hou, J.-J.; Liang, Q.-M.; Liao, H.; Huang, S.-F.; Yu, B. A Proposed Global Layout of Carbon Capture and Storage in Line with a 2 °C Climate Target. *Nat. Clim. Chang.* **2021**, *11* (2), 112–118.
- (7) Mertens, J.; Breyer, C.; Arning, K.; Bardow, A.; Belmans, R.; Dibenedetto, A.; Erkman, S.; Griepkoven, J.; Léonard, G.; Nizou, S.; Pant, D.; Reis-Machado, A. S.; Styring, P.; Vente, J.; Webber, M.; Sapart, C. J. Carbon Capture and Utilization: More than Hiding CO₂ for Some Time. *Joule* **2023**, 1–8.
- (8) Hori, Y.; Wakebe, H. H. I.; Tsukamoto, T.; Koga, O. Electrocatalytic Process of CO Selectivity in Electrochemical Reduction of CO₂ at Metal Electrodes in Aqueous Media. *Electrochim. Acta* **1994**, *39* (11–12), 1833–1839.
- (9) Bushuyev, O. S.; De Luna, P.; Dinh, C. T.; Tao, L.; Saur, G.; van de Lagemaat, J.; Kelley, S. O.; Sargent, E. H. What Should We Make with CO₂ and How Can We Make It? *Joule* **2018**, *2* (5), 825–832.
- (10) Chen, C.; Khosrowabadi Kotyk, J. F.; Sheehan, S. W. Progress toward Commercial Application of Electrochemical Carbon Dioxide Reduction. *Chem* **2018**, *4* (11), 2571–2586.
- (11) Debergh, P.; Gutiérrez-Sánchez, O.; Khan, M. N.; Birdja, Y. Y.; Pant, D.; Bulut, M. The Economics of Electrochemical Syngas Production via Direct Air Capture. *ACS Energy Lett.* **2023**, *8* (8), 3398–3403.
- (12) Ramdin, M.; Morrison, A. R. T.; De Groen, M.; Van Haperen, R.; De Kler, R.; Irtem, E.; Laitinen, A. T.; Van Den Broeke, L. J. P.; Breugelmans, T.; Trusler, J. P. M.; Jong, W. De; Vlugt, T. J. H. High-Pressure Electrochemical Reduction of CO₂ to Formic Acid/Formate: Effect of PH on the Downstream Separation Process and Economics. *Ind. Eng. Chem. Res.* **2019**, *58* (51), 22718–22740.
- (13) An, X.; Li, S.; Hao, X.; Xie, Z.; Du, X.; Wang, Z.; Hao, X.; Abudula, A.; Guan, G. Common Strategies for Improving the Performances of Tin and Bismuth-Based Catalysts in the Electrocatalytic

- Reduction of CO₂ to Formic Acid/Formate. *Renewable Sustainable Energy Rev.* **2021**, *143* (February), 110952.
- (14) Yang, Z.; Oropeza, F. E.; Zhang, K. H. L. P-Block Metal-Based (Sn, In, Bi, Pb) Electrocatalysts for Selective Reduction of CO₂ to Formate. *APL Mater.* **2020**, *8* (6), 060901.
- (15) Ding, P.; Zhao, H.; Li, T.; Luo, Y.; Fan, G.; Chen, G.; Gao, S.; Shi, X.; Lu, S.; Sun, X. Metal-Based Electrocatalytic Conversion of CO₂ to Formic Acid/Formate. *J. Mater. Chem. A* **2020**, *8* (42), 21947–21960.
- (16) Masel, R. I.; Liu, Z.; Yang, H.; Kaczur, J. J.; Carrillo, D.; Ren, S.; Salvatore, D.; Berlinguette, C. P. An Industrial Perspective on Catalysts for Low-Temperature CO₂ Electrolysis. *Nat. Nanotechnol.* **2021**, *16* (2), 118–128.
- (17) Kibria, M. G.; Edwards, J. P.; Gabardo, C. M.; Dinh, C. T.; Seifitokaldani, A.; Sinton, D.; Sargent, E. H. Electrochemical CO₂ Reduction into Chemical Feedstocks: From Mechanistic Electrocatalysis Models to System Design. *Adv. Mater.* **2019**, *31* (31), 1–24.
- (18) Zhao, S.; Li, S.; Guo, T.; Zhang, S.; Wang, J.; Wu, Y.; Chen, Y. Advances in Sn-Based Catalysts for Electrochemical CO₂ Reduction. *Nanomicro Lett.* **2019**, *11* (1), 62.
- (19) Sun, Z.; Ma, T.; Tao, H.; Fan, Q.; Han, B. Fundamentals and Challenges of Electrochemical CO₂ Reduction Using Two-Dimensional Materials. *Chem.* **2017**, *3* (4), 560–587.
- (20) Deng, W.; Zhang, P.; Seger, B.; Gong, J. Unraveling the Rate-Limiting Step of Two-Electron Transfer Electrochemical Reduction of Carbon Dioxide. *Nat. Commun.* **2022**, *13* (1), 803.
- (21) Goel, C.; Bhunia, H.; Bajpai, P. K. Synthesis of Nitrogen Doped Mesoporous Carbons for Carbon Dioxide Capture. *RSC Adv.* **2015**, *5* (58), 46568–46582.
- (22) Wan, X.; Li, Y.; Xiao, H.; Pan, Y.; Liu, J. Hydrothermal Synthesis of Nitrogen-Doped Ordered Mesoporous Carbon via Lysine-Assisted Self-Assembly for Efficient CO₂ Capture. *RSC Adv.* **2020**, *10* (5), 2932–2941.
- (23) Chen, J.; Wu, Q.; Mi, J.; Fan, C.; Wang, Z.; Chen, X.; Wang, G.; Huang, Z.; Li, J. Efficient and Simple Strategy to Obtain Ordered Mesoporous Carbons with Abundant Structural Base N Sites toward CO₂ Selective Capture and Catalytic Conversion. *ACS Sustain. Chem. Eng.* **2022**, *10* (16), 5175–5182.
- (24) Fu, Y.; Wang, T.; Zheng, W.; Lei, C.; Yang, B.; Chen, J.; Li, Z.; Lei, L.; Yuan, C.; Hou, Y. Nanoconfined Tin Oxide within N-Doped Nanocarbon Supported on Electrochemically

- Exfoliated Graphene for Efficient Electroreduction of CO₂ to Formate and C₁ Products. *ACS Appl. Mater. Interfaces* **2020**, *12* (14), 16178–16185.
- (25) Varela, A. S.; Ju, W.; Bagger, A.; Franco, P.; Rossmeisl, J.; Strasser, P. Electrochemical Reduction of CO₂ on Metal-Nitrogen-Doped Carbon Catalysts. *ACS Catal.* **2019**, *9* (8), 7270–7284.
- (26) Van Daele, K.; De Mot, B.; Pupo, M.; Daems, N.; Pant, D.; Kortlever, R.; Breugelmans, T. Sn-Based Electrocatalyst Stability: A Crucial Piece to the Puzzle for the Electrochemical CO₂ Reduction toward Formic Acid. *ACS Energy Lett.* **2021**, *6* (12), 4317–4327.
- (27) Zhang, R.; Lv, W.; Li, G.; Lei, L. Electrochemical Reduction of CO₂ on SnO₂/Nitrogen-Doped Multiwalled Carbon Nanotubes Composites in KHCO₃ Aqueous Solution. *Mater. Lett.* **2015**, *141*, 63–66.
- (28) Birdja, Y. Y.; Shen, J.; Koper, M. T. M. Influence of the Metal Center of Metalloprotoporphyrins on the Electrocatalytic CO₂ Reduction to Formic Acid. *Catal. Today* **2017**, *288*, 37–47.
- (29) Zhao, Y.; Liang, J.; Wang, C.; Ma, J.; Wallace, G. G. Tunable and Efficient Tin Modified Nitrogen-Doped Carbon Nanofibers for Electrochemical Reduction of Aqueous Carbon Dioxide. *Adv. Energy Mater.* **2018**, *8* (10), 1702524.
- (30) Duarte, M.; Daems, N.; Hereijgers, J.; Arenas-Esteban, D.; Bals, S.; Breugelmans, T. Enhanced CO₂ Electroreduction with Metal-Nitrogen-Doped Carbons in a Continuous Flow Reactor. *J. CO₂ Util.* **2021**, *50* (May), 101583.
- (31) Sheng, X.; Daems, N.; Geboes, B.; Kurttepel, M.; Bals, S.; Breugelmans, T.; Hubin, A.; Vankelecom, I. F. J.; Pescarmona, P. P. N-Doped Ordered Mesoporous Carbons Prepared by a Two-Step Nanocasting Strategy as Highly Active and Selective Electrocatalysts for the Reduction of O₂ to H₂O₂. *Appl. Catal. B* **2015**, *176–177* (2015), 212–224.
- (32) Daems, N.; Risplendi, F.; Baert, K.; Hubin, A.; Vankelecom, I. F. J.; Cicero, G.; Pescarmona, P. P. Doped Ordered Mesoporous Carbons as Novel, Selective Electrocatalysts for the Reduction of Nitrobenzene to Aniline. *J. Mater. Chem. A* **2018**, *6* (27), 13397–13411.
- (33) Wang, Y.; Li, B.; Zhang, C.; Tao, H.; Kang, S.; Jiang, S.; Li, X. Simple Synthesis of Metallic Sn Nanocrystals Embedded in Graphitic Ordered Mesoporous Carbon Walls as Superior Anode Materials for Lithium Ion Batteries. *J. Power Sources* **2012**, *219*, 89–93.
- (34) Schlossmacher, P.; Klenov, D. O.; Freitag, B.; von Harrach, H. S. Enhanced Detection Sensitivity with a New Windowless XEDS System for AEM Based on Silicon Drift Detector Technology. *Microsc. Today* **2010**, *18* (4), 14–20.

- (35) Thommes, M.; Kaneko, K.; Neimark, A. V.; Olivier, J. P.; Rodriguez-Reinoso, F.; Rouquerol, J.; Sing, K. S. W. Physisorption of Gases, with Special Reference to the Evaluation of Surface Area and Pore Size Distribution (IUPAC Technical Report). *Pure Appl. Chem.* **2015**, *87* (9–10), 1051–1069.
- (36) Ferrari, A. C.; Basko, D. M. Raman Spectroscopy as a Versatile Tool for Studying the Properties of Graphene. *Nat. Nanotechnol.* **2013**, *8* (4), 235–246.
- (37) Schuepfer, D. B.; Badaczewski, F.; Guerra-Castro, J. M.; Hofmann, D. M.; Heiliger, C.; Smarsly, B.; Klar, P. J. Assessing the Structural Properties of Graphitic and Non-Graphitic Carbons by Raman Spectroscopy. *Carbon* **2020**, *161*, 359–372.
- (38) Graulis, S.; Chateigner, D.; Downs, R. T.; Yokochi, A. F. T.; Quirós, M.; Lutterotti, L.; Manakova, E.; Butkus, J.; Moeck, P.; Le Bail, A. Crystallography Open Database - An Open-Access Collection of Crystal Structures. *J. Appl. Crystallogr.* **2009**, *42* (4), 726–729.
- (39) Seki, H.; Ishizawa, N.; Mizutani, N.; Kato, M. High Temperature Structures of the Rutile-Type Oxides, TiO₂ and SnO₂. *Journal of the Ceramic Association, Japan* **1984**, *92* (1064), 219–223.
- (40) Hursán, D.; Samu, A. A.; Janovák, L.; Artyushkova, K.; Asset, T.; Atanassov, P.; Janáky, C. Morphological Attributes Govern Carbon Dioxide Reduction on N-Doped Carbon Electrodes. *Joule* **2019**, *3* (7), 1719–1733.
- (41) Van den Hoek, J.; Daems, N.; Arnouts, S.; Hoekx, S.; Bals, S.; Breugelmans, T. Improving Stability of CO₂ Electroreduction by Incorporating Ag NPs in N-Doped Ordered Mesoporous Carbon Structures. *ACS Appl. Mater. Interfaces* **2024**, *16* (6), 6931–6947.
- (42) Wu, J.; Sun, S.-G.; Zhou, X.-D. Origin of the Performance Degradation and Implementation of Stable Tin Electrodes for the Conversion of CO₂ to Fuels. *Nano Energy* **2016**, *27*, 225–229.
- (43) Daele, K. Van; Arenas-Esteban, D.; Choukroun, D.; Hoekx, S.; Rossen, A.; Daems, N.; Pant, D.; Bals, S.; Breugelmans, T. Enhanced Pomegranate-Structured SnO₂ Electrocatalysts for the Electrochemical CO₂ Reduction to Formate. *ChemElectroChem* **2023**, *202201024*, 1–9.
- (44) Wyckoff, R. W. G. Second Edition. Interscience Publishers, New York, New York Sample Known as White Tin. *Crystal Structures* **1963**, *1*, 7–83.
- (45) Thomas, J. O.; Tellgren, R.; Olovsson, I. Hydrogen Bond Studies. LXXXIV. An X-Ray Diffraction Study of the Structures of KHCO₃ and KD₂CO₃ at 298, 219 and 95 K. *Acta. Crystallogr. B* **1974**, *30* (5), 1155–1166.

- (46) Cheng, D.; Zhao, Z. J.; Zhang, G.; Yang, P.; Li, L.; Gao, H.; Liu, S.; Chang, X.; Chen, S.; Wang, T.; Ozin, G. A.; Liu, Z.; Gong, J. The Nature of Active Sites for Carbon Dioxide Electroreduction over Oxide-Derived Copper Catalysts. *Nat. Commun.* **2021**, *12* (1).
- (47) Bagchi, D.; Sarkar, S.; Singh, A. K.; Vinod, C. P.; Peter, S. C. Potential- and Time-Dependent Dynamic Nature of an Oxide-Derived PdIn Nanocatalyst during Electrochemical CO₂ Reduction. *ACS Nano* **2022**, *16* (4), 6185–6196.
- (48) Baruch, M. F.; Pander, J. E.; White, J. L.; Bocarsly, A. B. Mechanistic Insights into the Reduction of CO₂ on Tin Electrodes Using in Situ ATR-IR Spectroscopy. *ACS Catal.* **2015**, *5* (5), 3148–3156.

Synergy or Antagonism? Exploring the Interplay of SnO₂ and an N-OMC Carbon Capture Medium for the Electrochemical CO₂ Reduction Towards Formate

Supporting Information

Kevin Van Daele^{a, b}, Deema Balalta^c, Saskia Hoekx^{a, c}, Robbe Jacobs^{a, e}, Dr. Nick Daems^a, Dr. Thomas Altantzis^a, Dr. Deepak Pant^{b, d}, Prof. Dr. Tom Breugelmans*^{a, d}

a) Applied Electrochemistry & Catalysis (ELCAT), University of Antwerp, Universiteitsplein 1, 2610 Wilrijk, Belgium

b) Electrochemistry Excellence Centre, Materials & Chemistry unit, Flemish Institute for Technological Research (VITO), Boeretang 200, 2400 Mol, Belgium

c) Electron Microscopy for Materials Science (EMAT), University of Antwerp, Groenenborgerlaan 171, 2020 Antwerp, Belgium

d) Center for Advanced Process Technology for Urban Resource Recovery (CAPTURE), Frieda Saeystraat 1, 9052 Zwijnaarde, Belgium

e) Design & Synthesis of Inorganic materials for Energy applications (DESINe), University of Hasselt, Agoralaan, 3590 Diepenbeek, Belgium

*corresponding author: tom.breugelmans@uantwerpen.be

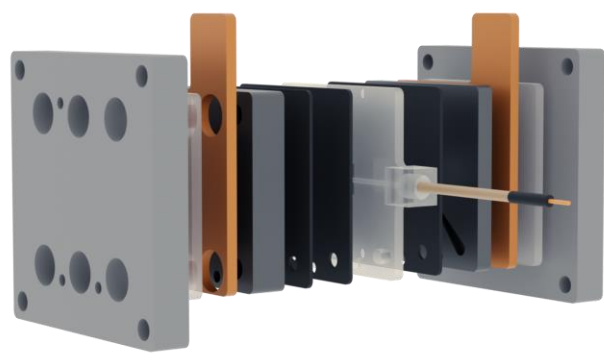
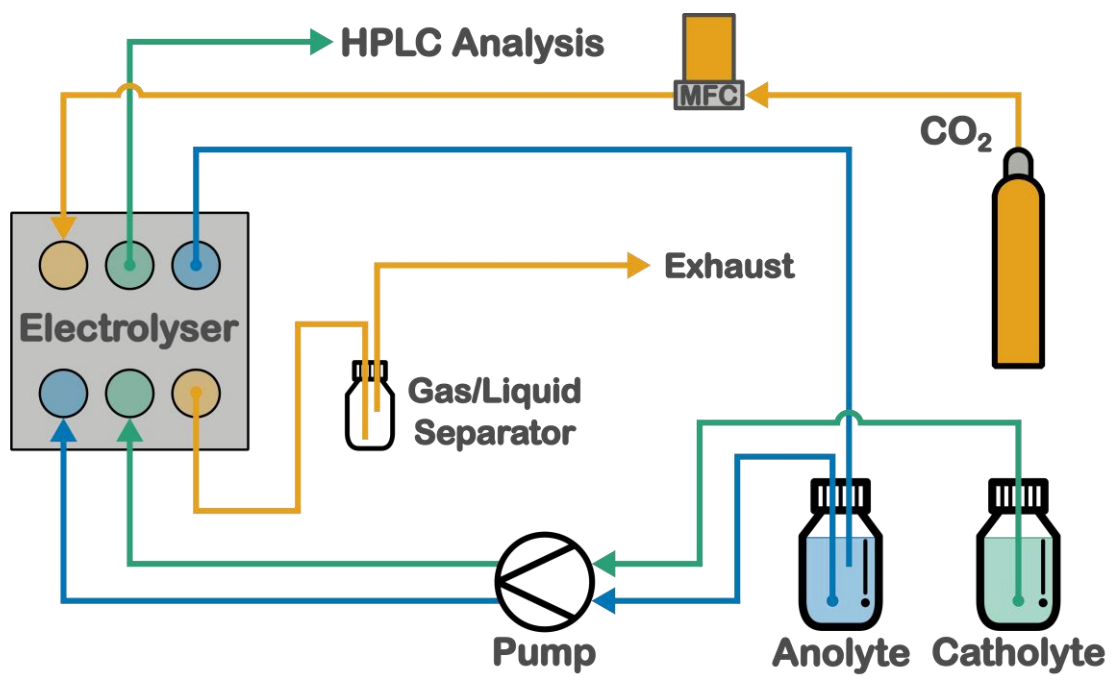


Figure S1. eCO₂R electrolyser setup

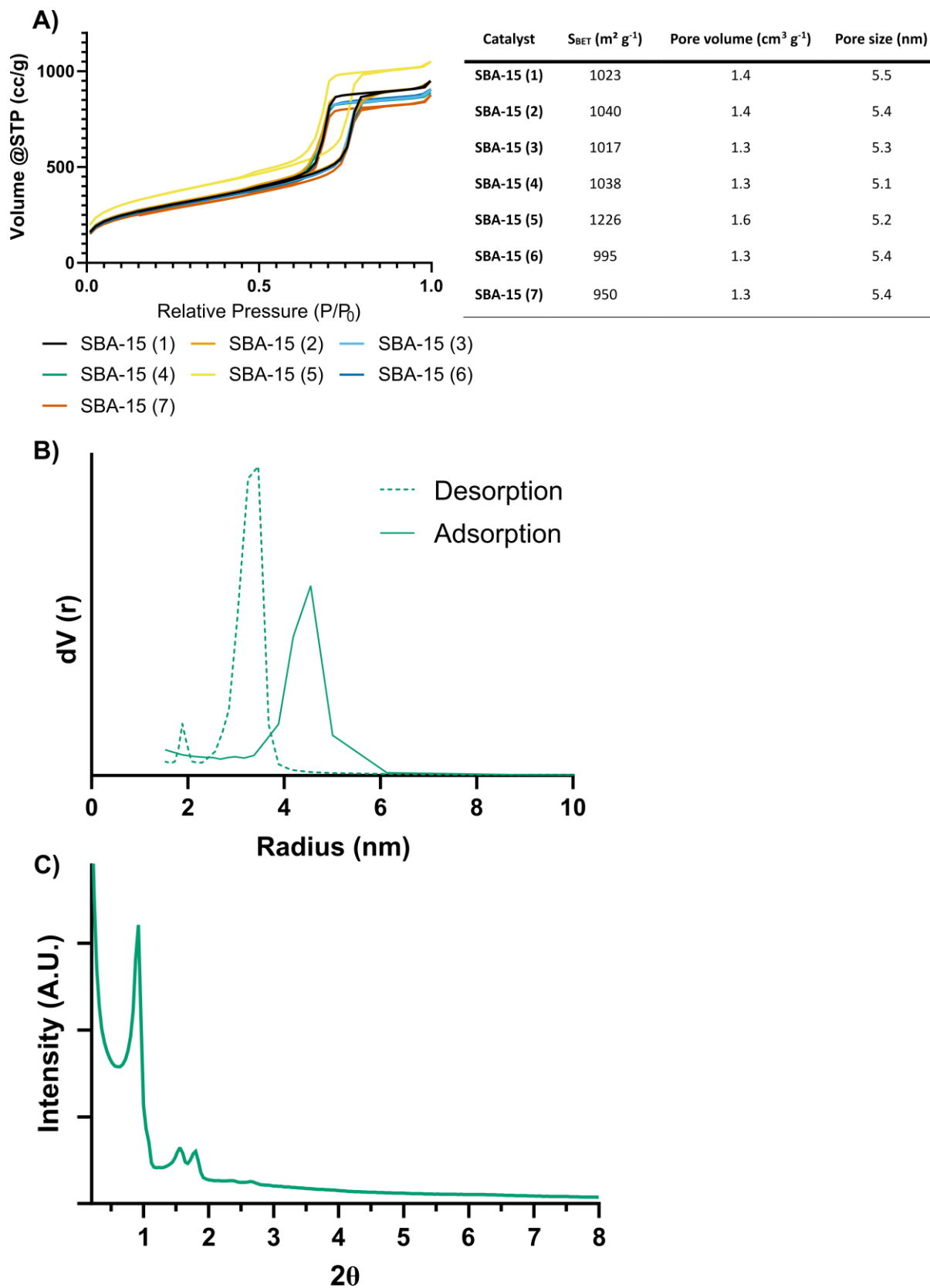
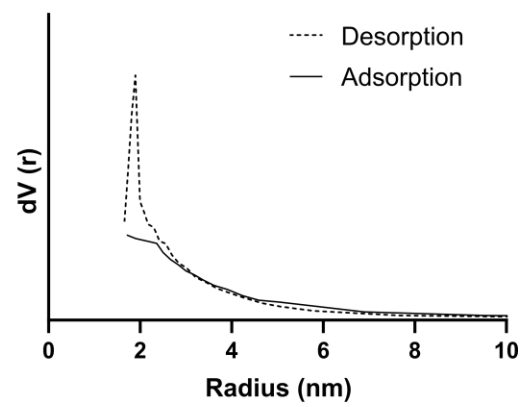
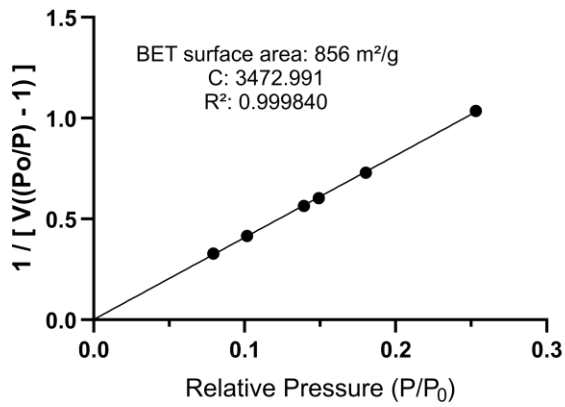
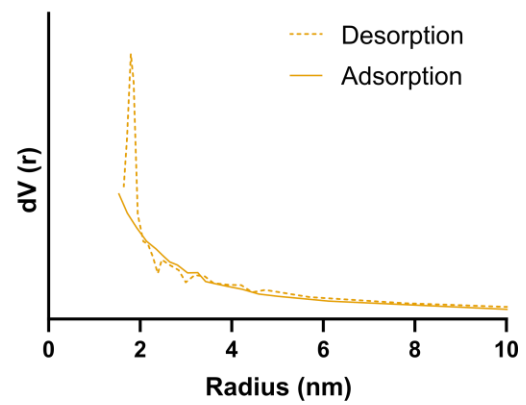
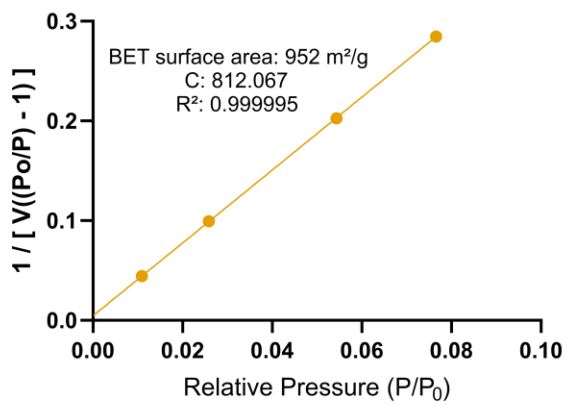


Figure S2. Physicochemical characterization SBA-15 with A) nitrogen adsorption-desorption isotherms of all SBA-15 samples, B) BJH pore size distribution of SBA-15 (4) and C) Low Angle XRD of SBA-15 (4)

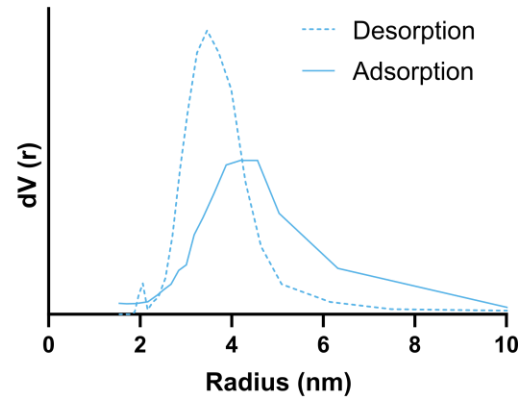
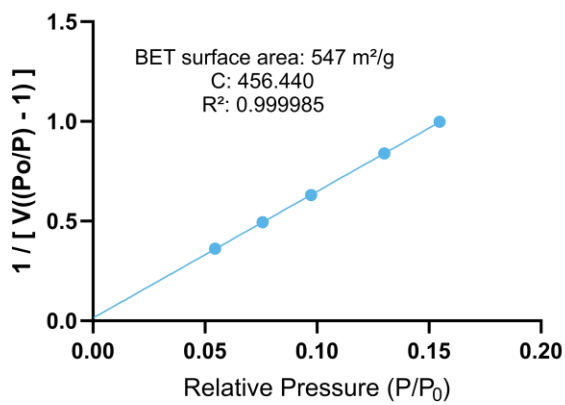
N-OMC (1)



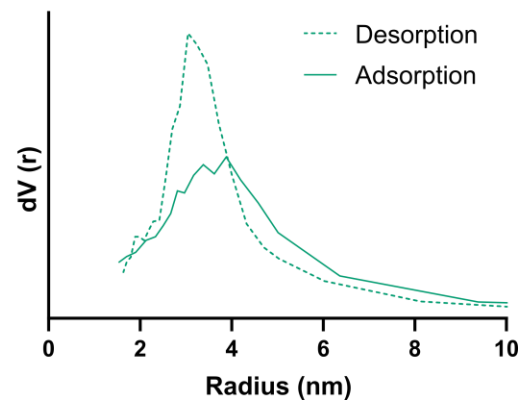
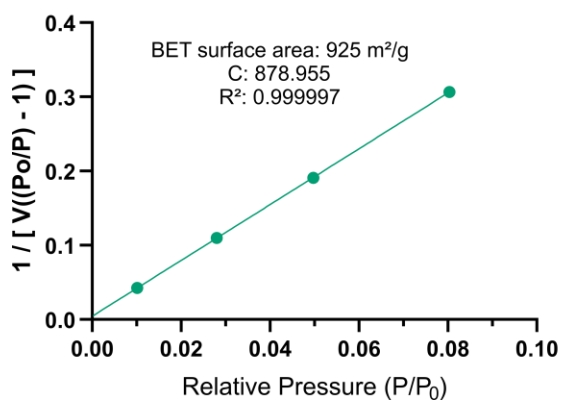
SnO₂-N-OMC (1)



SnO₂-N-OMC (2)



SnO₂-N-OMC (3)



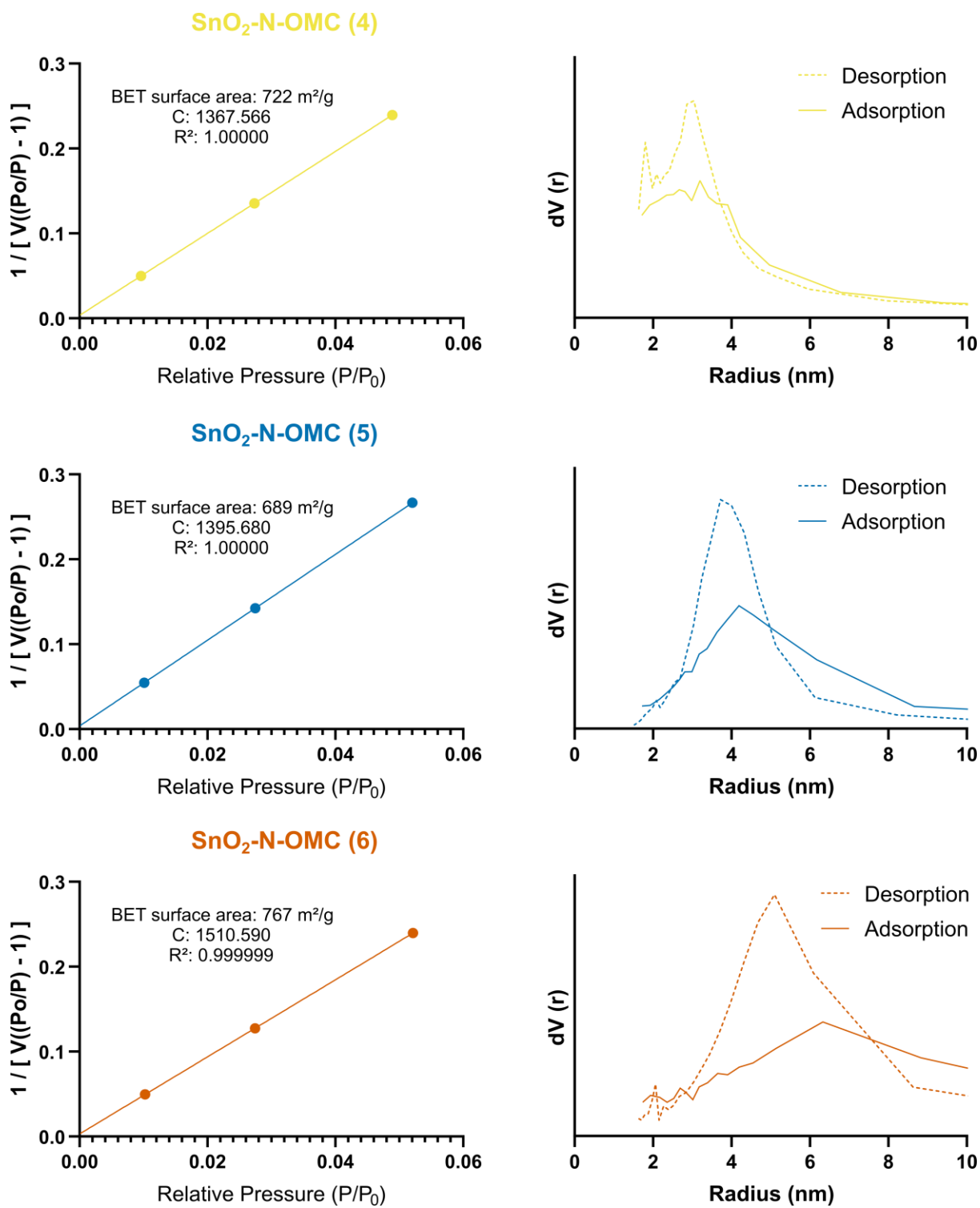


Figure S3. BET surface area and pore size distribution plots of all (SnO₂-)N-OMC electrocatalysts

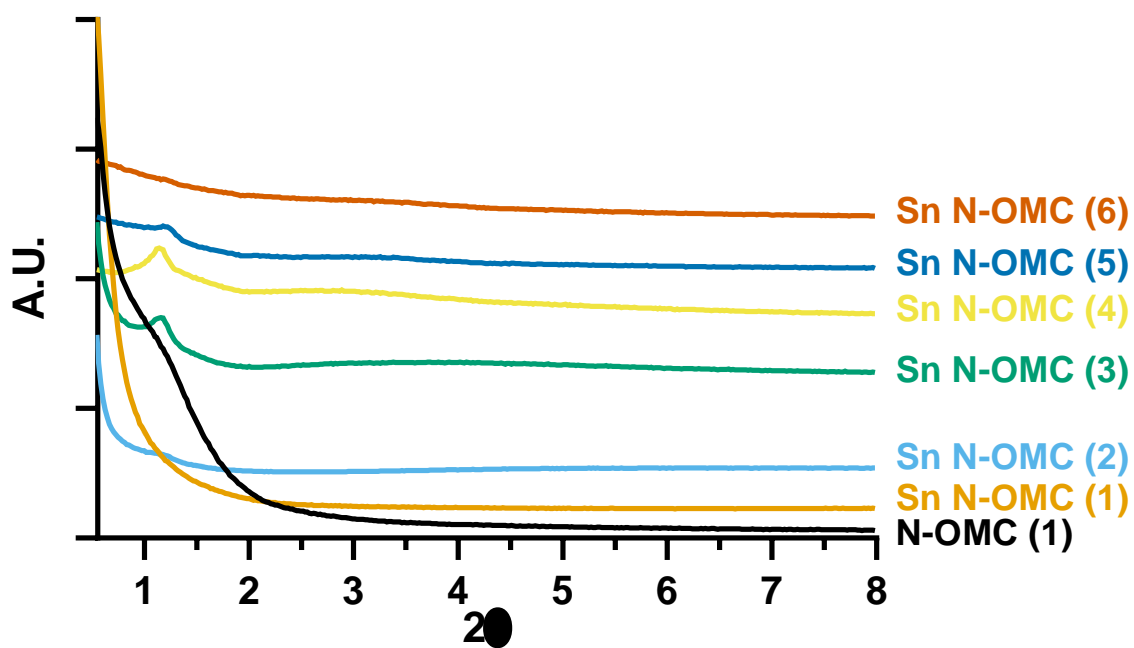


Figure S4. Low Angle XRD (SnO_2)-N-OMC electrocatalysts

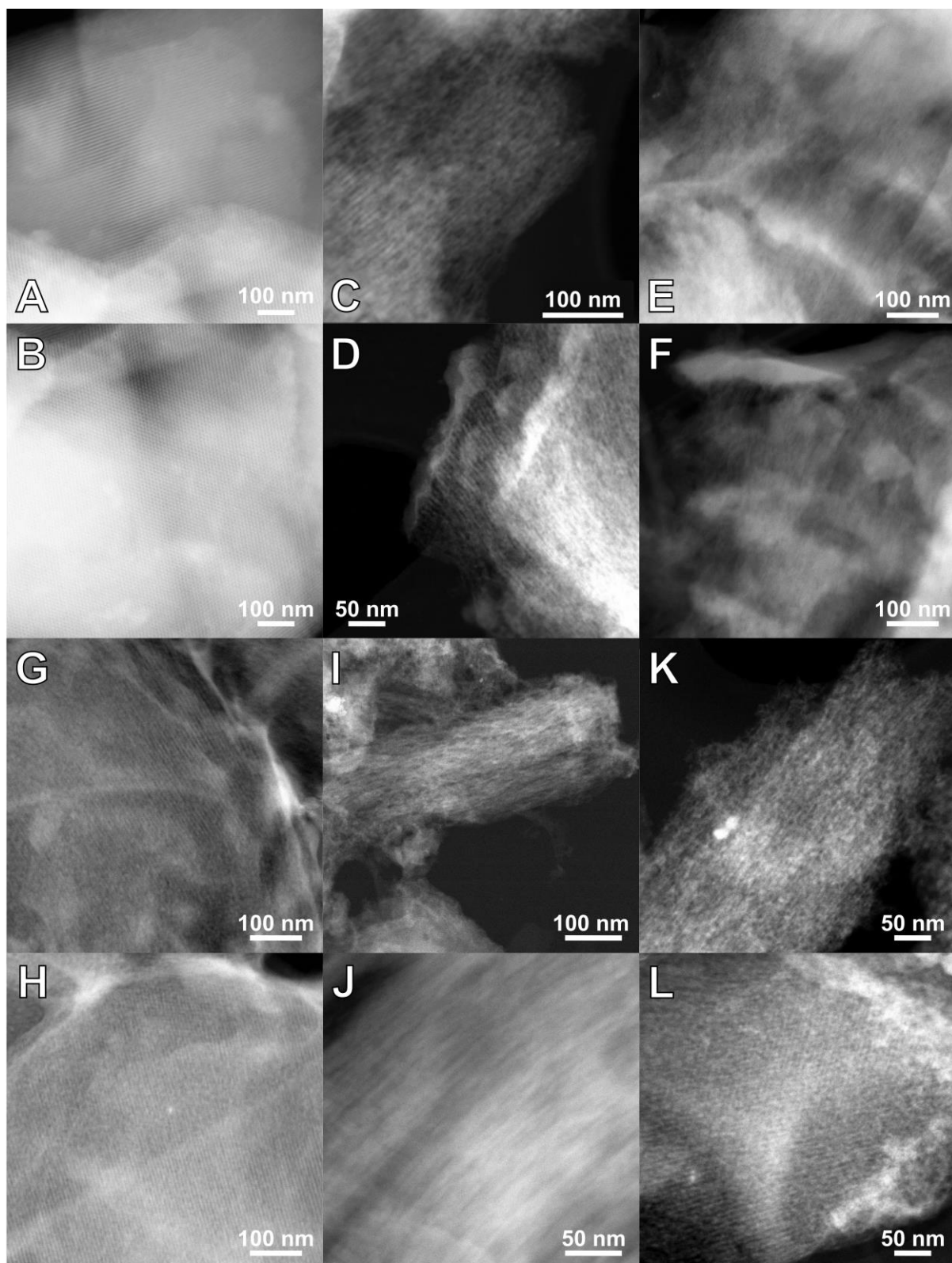


Figure S5. HAADF STEM images of A, B) SBA-15; C, D) N-OMC (1); E, F) SnO₂-N-OMC (1); G, H) SnO₂-N-OMC (2); I, J) SnO₂-N-OMC (4) and K, L) SnO₂-N-OMC (6)

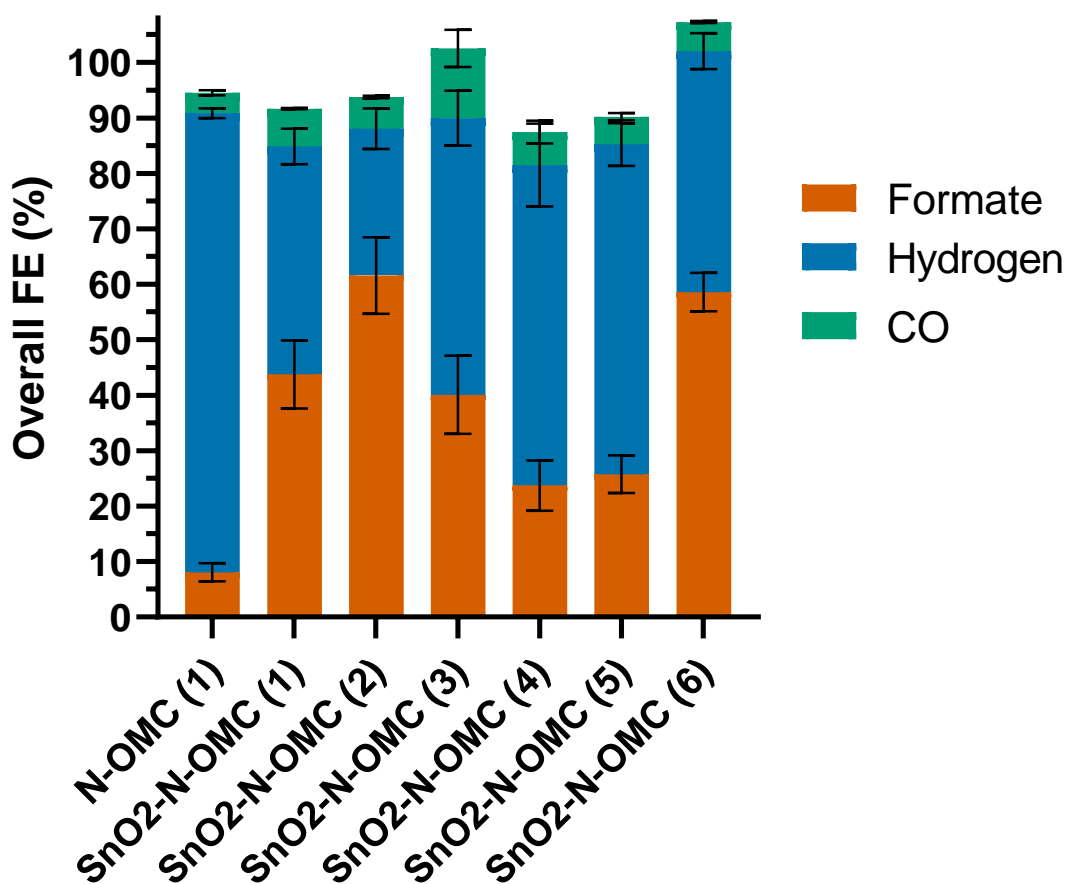


Figure S6. Overall average FE% for all seven electrocatalysts, measured at a constant current density of 100 mA cm^{-2} for 1 h.

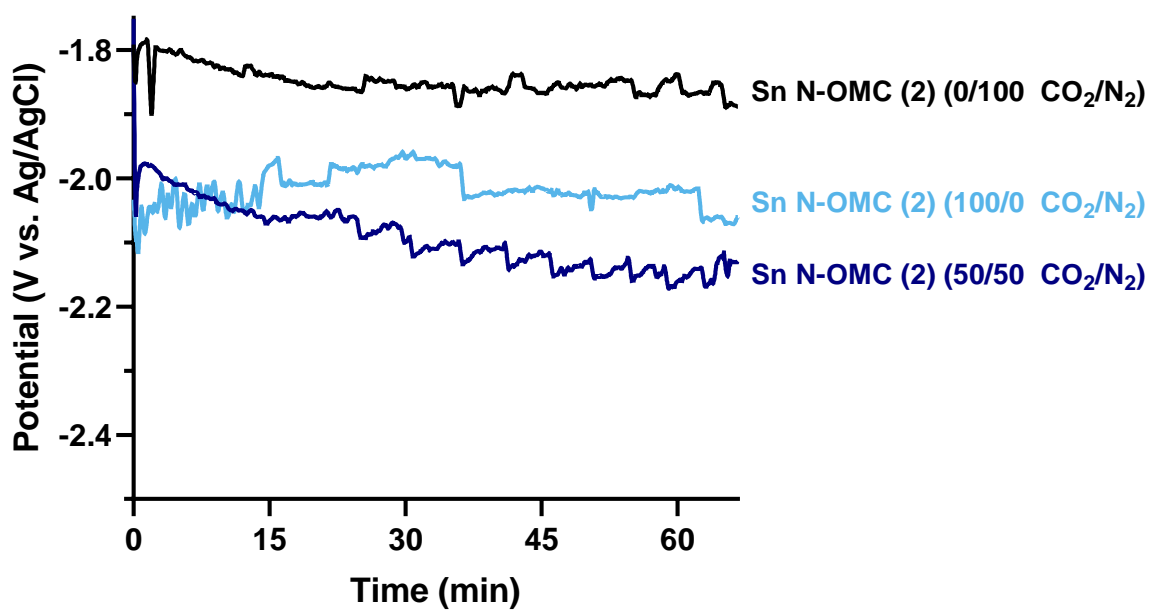


Figure S7. Uncompensated potential (V vs. Ag/AgCl) as a function of time at a constant current density of 100 mA cm^{-2} for 1 h, with varying CO₂/N₂ concentrations.

Table S1. State-of-the-art Sn-based and N-doped Sn-based electrocatalysts

Catalyst	FE _{FA} (%)	Working Potential (V) vs. RHE	J (mA cm ⁻²)	Stability (h)	Electrolyte	Ref.
Bi _{0.1} Sn*	95	-0.65	100	2400	1.0 M KHCO ₃	1
Sn nanoparticles GDE*	94	-1.48	140	550	DI water	2
SnO ₂ GDE*	70	-1.40	12	174	0.1 M KHCO ₃	3
SnO ₂ /γ-Al ₂ O ₃	65	-1.37	21.7	152	0.5 M KHCO ₃	4
Bi-Sn/CF	96	-1.14	45	100	0.5 M KHCO ₃	5
SnDT GDE*	62.5	-0.76	18.7	72	1.0 M KHCO ₃	6
SnIn-3	84.6	-1.0	39	58	0.1 M KHCO ₃	7
np-Sn/SnO ₂	80	-1.1	16	58	0.5 M NaHCO ₃	8
p-SnS _x	97	-1.0	15	50	0.1 M KHCO ₃	9
CuSn ₃	95	-0.5	33	50	0.1 M KHCO ₃	10
Sn _{0.80} Bi _{0.20} @Bi-SnO _x *	>90	-0.88	20.9	50	0.5 M KHCO ₃	11
Sn quantum sheets/GO	85	-1.16	21	50	0.1 M KHCO ₃	12
SnO _x NP-s*	81	-1.20	9.03	50	0.1 M KHCO ₃	13
CuSn-10C	82	-1.0	18.9	42	0.1 M NaHCO ₃	14
Sn(S)/Au	93	-0.75	55	40	0.1 M KHCO ₃	15
Sn _{2.7} Cu GDE*	90	-0.55	243.1	40	1.0 M KOH	16
Pomegranate SnO ₂ @C	85	-0.70	100	24	0.5 M KHCO ₃	17
Pomegranate SnO ₂	80	-0.62	100	24	0.5 M KHCO ₃	17
Commercial SnO ₂ NPs	79	-0.50	100	24	0.5 M KHCO ₃	17
SnO ₂ /CC	87	-0.97	50	24	0.5 M NaHCO ₃	18
Ag ₇₆ Sn ₂₄ /SnO _x	80	-0.8	19.7	24	0.5 M NaHCO ₃	19
Sn-N-C	70	/	100	24	0.5 M KHCO ₃	20
Sn-CF1000	63	-0.8	16.6	24	0.5 M KHCO ₃	21
SnO₂-N-OMC (2)*	62	-0.54	100	24	0.5 M KHCO₃	This Work
SnO₂-N-OMC (6)*	58.6	-0.42	100	1	0.5 M KHCO₃	This Work
SnO₂▷NC@EEG	81.2	-1.2	11	10	0.1 M KHCO ₃	22
SnO₂/N-MWCNTs	46	-0.9 V vs. Ag/AgCl	> 1	10	0.1 M KHCO ₃	23

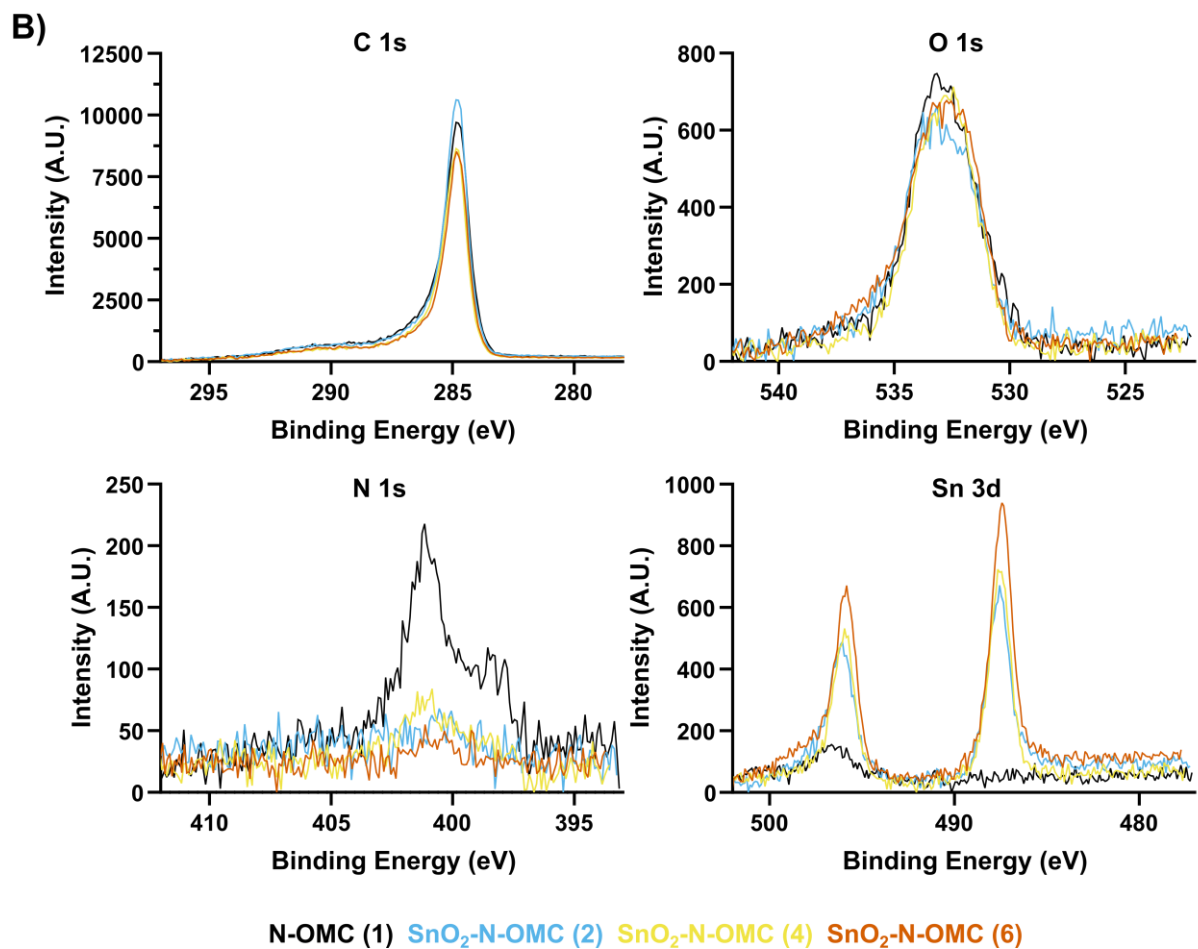
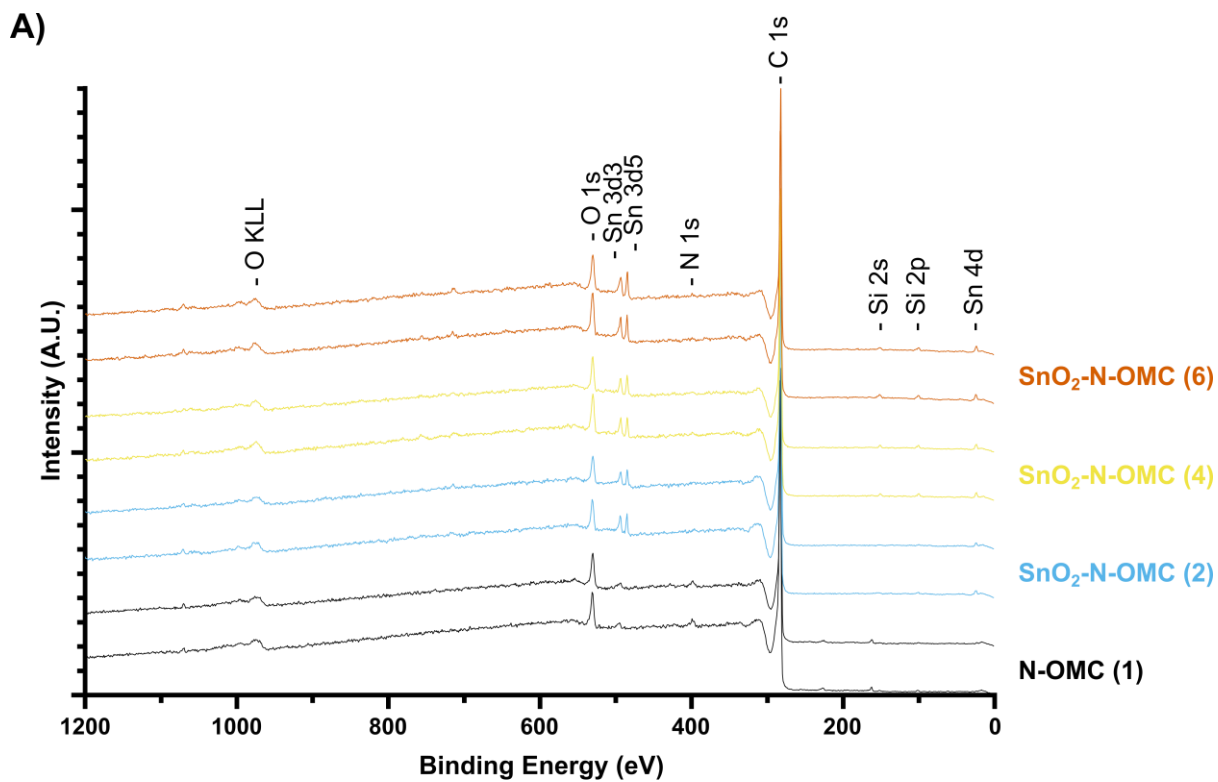


Figure S8. XPS spectra N-OMC (1), SnO₂-N-OMC (2), SnO₂-N-OMC (4) and SnO₂-N-OMC (6), with A) duplicate survey of all (Sn-)N-OMC electrocatalysts and B) high resolution spectra of C 1s, O 1s, N 1s and Sn 3d

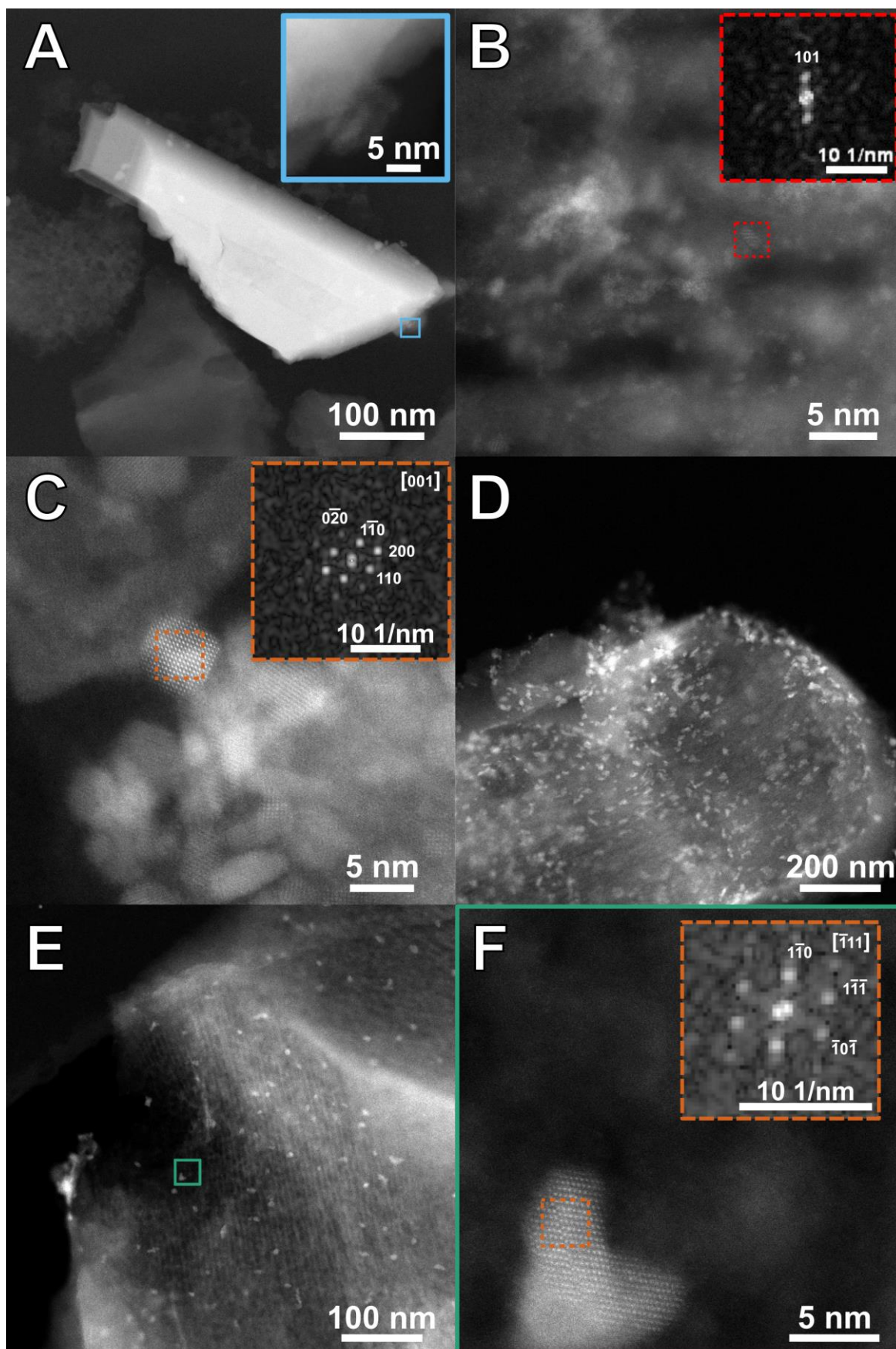


Figure S9. HAADF STEM images and the corresponding Fourier Transform (FT) patterns of A) an irregular large SnO_2 species and B) atomically dispersed species, presumed to be Sn-based and C) SnO_2 nanoparticles in SnO_2 -N-OMC (2); D, E and F) SnO_2 nanoparticles in SnO_2 -N-OMC (6).

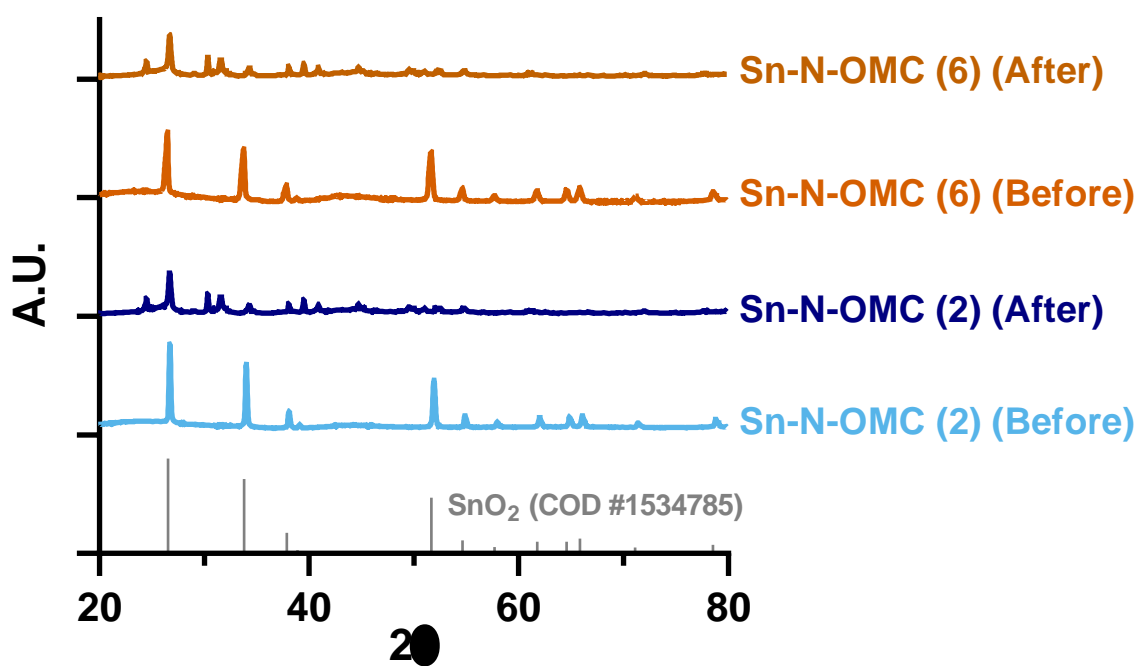


Figure S10. Wide angle X-ray diffractogram of the as-synthesized SnO₂-N-OMC electrocatalysts, before and after 24h of eCO₂R, compared with the Crystallography Open Database (COD) #1534785 for tetragonal SnO₂.

- (1) Li, L.; Ozden, A.; Guo, S.; García de Arquer, F. P.; Wang, C.; Zhang, M.; Zhang, J.; Jiang, H.; Wang, W.; Dong, H.; Sinton, D.; Sargent, E. H.; Zhong, M. Stable, Active CO₂ Reduction to Formate via Redox-Modulated Stabilization of Active Sites. *Nat. Commun.* **2021**, *12* (1), 5223.
- (2) Yang, H.; Kaczur, J. J.; Sajjad, S. D.; Masel, R. I. Electrochemical Conversion of CO₂ to Formic Acid Utilizing Sustainion™ Membranes. *Journal of CO₂ Utilization* **2017**, *20* (February), 208–217.
- (3) Wu, J.; Sun, S.-G.; Zhou, X.-D. Origin of the Performance Degradation and Implementation of Stable Tin Electrodes for the Conversion of CO₂ to Fuels. *Nano Energy* **2016**, *27*, 225–229.
- (4) Kim, Y. E.; Lee, W.; Youn, M. H.; Jeong, S. K.; Kim, H. J.; Park, J. C.; Park, K. T. Leaching-Resistant SnO₂/γ-Al₂O₃ Nanocatalyst for Stable Electrochemical CO₂ Reduction into Formate. *Journal of Industrial and Engineering Chemistry* **2019**, *78*, 73–78.
- (5) Wen, G.; Lee, D. U.; Ren, B.; Hassan, F. M.; Jiang, G.; Cano, Z. P.; Gostick, J.; Croiset, E.; Bai, Z.; Yang, L.; Chen, Z. Orbital Interactions in Bi-Sn Bimetallic Electrocatalysts for Highly Selective Electrochemical CO₂ Reduction toward Formate Production. *Adv. Energy Mater.* **2018**, *8* (31), 1802427.
- (6) Lim, J.; Kang, P. W.; Jeon, S. S.; Lee, H. Electrochemically Deposited Sn Catalysts with Dense Tips on a Gas Diffusion Electrode for Electrochemical CO₂ Reduction. *J. Mater. Chem. A* **2020**, *8* (18), 9032–9038.
- (7) Wang, J.; Ning, S.; Luo, M.; Xiang, D.; Chen, W.; Kang, X.; Jiang, Z.; Chen, S. In-Sn Alloy Core-Shell Nanoparticles: In-Doped SnO_x Shell Enables High Stability and Activity towards Selective Formate Production from Electrochemical Reduction of CO₂. *Appl. Catal. B* **2021**, *288* (October 2020), 119979.
- (8) Liu, S.; Pang, F.; Zhang, Q.; Guo, R.; Wang, Z.; Wang, Y.; Zhang, W.; Ou, J. Stable Nanoporous Sn/SnO₂ Composites for Efficient Electroreduction of CO₂ to Formate over Wide Potential Range. *Appl. Mater. Today* **2018**, *13*, 135–143.
- (9) Wang, X.; Liu, S.; Zhang, H.; Zhang, S.; Meng, G.; Liu, Q.; Sun, Z.; Luo, J.; Liu, X. Polycrystalline SnS_x Nanofilm Enables CO₂ Electroreduction to Formate with High Current Density. *Chemical Communications* **2022**, *58* (55), 7654–7657.
- (10) Zheng, X.; Ji, Y.; Tang, J.; Wang, J.; Liu, B.; Steinrück, H. G.; Lim, K.; Li, Y.; Toney, M. F.; Chan, K.; Cui, Y. Theory-Guided Sn/Cu Alloying for Efficient CO₂ Electroreduction at Low Overpotentials. *Nat. Catal.* **2019**, *2* (1), 55–61.

- (11) Yang, Q.; Wu, Q.; Liu, Y.; Luo, S.; Wu, X.; Zhao, X.; Zou, H.; Long, B.; Chen, W.; Liao, Y.; Li, L.; Shen, P. K.; Duan, L.; Quan, Z. Novel Bi-Doped Amorphous SnO_x Nanoshells for Efficient Electrochemical CO₂ Reduction into Formate at Low Overpotentials. *Advanced Materials* **2020**, *32* (36), 1–7.
- (12) Lei, F.; Liu, W.; Sun, Y.; Xu, J.; Liu, K.; Liang, L.; Yao, T.; Pan, B.; Wei, S.; Xie, Y. Metallic Tin Quantum Sheets Confined in Graphene toward High-Efficiency Carbon Dioxide Electroreduction. *Nat. Commun.* **2016**, *7* (1), 12697.
- (13) Kim, M. K.; Lee, H.; Won, J. H.; Sim, W.; Kang, S. J.; Choi, H.; Sharma, M.; Oh, H.; Ringe, S.; Kwon, Y.; Jeong, H. M. Design of Less than 1 Nm Scale Spaces on SnO₂ Nanoparticles for High-Performance Electrochemical CO₂ Reduction. *Adv. Funct. Mater.* **2022**, *32* (8), 2107349.
- (14) Wang, J.; Zou, J.; Hu, X.; Ning, S.; Wang, X.; Kang, X.; Chen, S. Heterostructured Intermetallic CuSn Catalysts: High Performance towards the Electrochemical Reduction of CO₂ to Formate. *J. Mater. Chem. A* **2019**, *7* (48), 27514–27521.
- (15) Zheng, X.; De Luna, P.; García de Arquer, F. P.; Zhang, B.; Becknell, N.; Ross, M. B.; Li, Y.; Banis, M. N.; Li, Y.; Liu, M.; Voznyy, O.; Dinh, C. T.; Zhuang, T.; Stadler, P.; Cui, Y.; Du, X.; Yang, P.; Sargent, E. H. Sulfur-Modulated Tin Sites Enable Highly Selective Electrochemical Reduction of CO₂ to Formate. *Joule* **2017**, *1* (4), 794–805.
- (16) Ye, K.; Zhou, Z.; Shao, J.; Lin, L.; Gao, D.; Ta, N.; Si, R.; Wang, G.; Bao, X. In Situ Reconstruction of a Hierarchical Sn-Cu/SnO_x Core/Shell Catalyst for High-Performance CO₂ Electroreduction. *Angewandte Chemie* **2020**, *132* (12), 4844–4851.
- (17) Daele, K. Van; Arenas-Esteban, D.; Choukroun, D.; Hoekx, S.; Rossen, A.; Daems, N.; Pant, D.; Bals, S.; Breugelmans, T. Enhanced Pomegranate-Structured SnO₂ Electrocatalysts for the Electrochemical CO₂ Reduction to Formate. *ChemElectroChem* **2023**, *202201024*, 1–9.
- (18) Li, F.; Chen, L.; Knowles, G. P.; MacFarlane, D. R.; Zhang, J. Hierarchical Mesoporous SnO₂ Nanosheets on Carbon Cloth: A Robust and Flexible Electrocatalyst for CO₂ Reduction with High Efficiency and Selectivity. *Angewandte Chemie - International Edition* **2017**, *56* (2), 505–509.
- (19) Luc, W.; Collins, C.; Wang, S.; Xin, H.; He, K.; Kang, Y.; Jiao, F. Ag-Sn Bimetallic Catalyst with a Core-Shell Structure for CO₂ Reduction. *J. Am. Chem. Soc.* **2017**, *139* (5), 1885–1893.

- (20) Duarte, M.; Daems, N.; Hereijgers, J.; Arenas-Esteban, D.; Bals, S.; Breugelmans, T. Enhanced CO₂ Electroreduction with Metal-Nitrogen-Doped Carbons in a Continuous Flow Reactor. *Journal of CO₂ Utilization* **2021**, *50* (May), 101583.
- (21) Zhao, Y.; Liang, J.; Wang, C.; Ma, J.; Wallace, G. G. Tunable and Efficient Tin Modified Nitrogen-Doped Carbon Nanofibers for Electrochemical Reduction of Aqueous Carbon Dioxide. *Adv. Energy Mater.* **2018**, *8* (10), 1–9.
- (22) Fu, Y.; Wang, T.; Zheng, W.; Lei, C.; Yang, B.; Chen, J.; Li, Z.; Lei, L.; Yuan, C.; Hou, Y. Nanoconfined Tin Oxide within N-Doped Nanocarbon Supported on Electrochemically Exfoliated Graphene for Efficient Electroreduction of CO₂ to Formate and C₁ Products. *ACS Appl. Mater. Interfaces* **2020**, *12* (14), 16178–16185.
- (23) Zhang, R.; Lv, W.; Li, G.; Lei, L. Electrochemical Reduction of CO₂ on SnO₂/Nitrogen-Doped Multiwalled Carbon Nanotubes Composites in KHCO₃ Aqueous Solution. *Mater. Lett.* **2015**, *141*, 63–66.